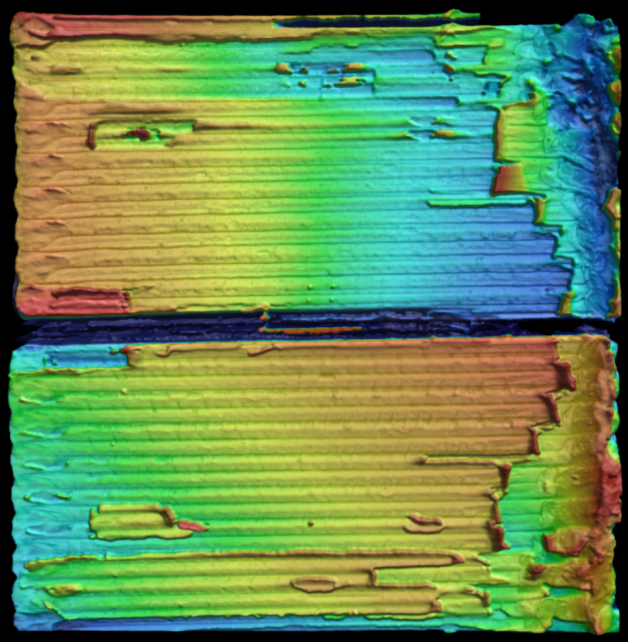

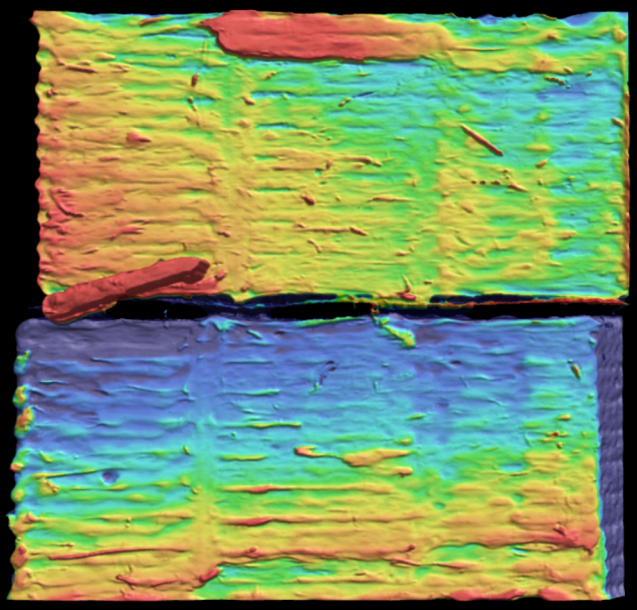

Interlaminar toughening approaches for additively manufactured liquid crystal polymers

Boris Ulyanov

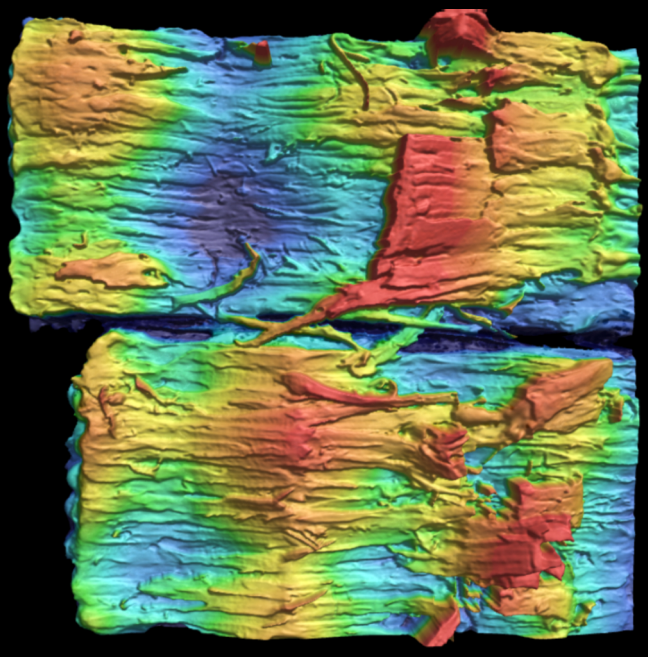

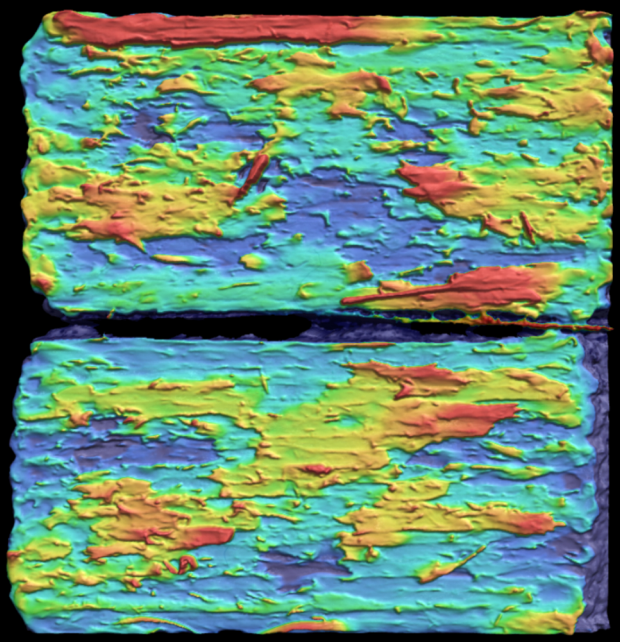

TU Delft

Interlaminar toughening approaches for additively manufactured liquid crystal polymers

by

Boris Ulyanov

Student number: 4672798

Thesis Commitee:	Dr. K. Masania,	TU Delft, Thesis Supervisor
	Dr. J.A. Pascoe,	TU Delft, Examiner
	Dr. C.A. Dransfeld,	TU Delft, Chair

TU Delft

Acknowledgements

This thesis has proven to be the biggest undertaking of my life so far. I needed to read many articles, fix many printing-related issues and run many analyses to get to where I am today. The difficulties of a research project predominantly focused on experimentation seemed insurmountable at times. However, the larger the obstacle, the more satisfying it is to overcome it, as I came to find out. Looking back at my work, I am proud to have persevered, and I am grateful for all the people who encouraged me along the way. There are many who helped me reach the end, but a few people were especially important, which is why they deserve their own mention.

First, I would like to thank my daily supervisor, Caroline Houriet. You have great insight into the worlds of liquid crystal polymers and additive manufacturing, and your tips were invaluable in the beginning when I was still a newbie. Your guidance was just as useful when I moved on to experiments, and I appreciate your help in setting them up. The feedback you gave when the report started to take shape was invaluable, and contributed to many changes for the better. Finally, thank you for always being so quick to answer my questions, and making me think in new and unorthodox ways.

Next, I want to thank my supervising professor, Dr. Kunal Masania. When I first met you during the Trinity Exercise, I did not suspect our cooperation would last as long as it has, but I am very glad that it did. Thank you for the great advice you provided me with throughout my whole thesis. Thank you for helping me find a good topic and for your input on interesting directions for it to take as it progressed. Most of all, thank you for introducing me to additive manufacturing and stoking my curiosity about this subject in the first place. I can safely say that you have left a mark on my future.

There are a few others in the Shaping Material Lab who I would also like to mention. Thanks to Vinay Damodaran for his advice regarding LCP. Thanks to Sander Wildenborg for the interesting conversations and for keeping me company in the lab. Finally, thanks to Guillermo Presa Magrina and Harold Rutten for being amazing colleagues and making my time in SML very enjoyable. Success with your projects, friends, and stay safe from Anna.

Last but not least, I would like to thank the most important people in my life (they know who they are). Thank you for all of your support and encouragement. Thank you for being at my side during this critical stage of my life. Lastly, thank you for believing in me.

Boris Ulyanov
November 1st, 2023

Abstract

Liquid crystalline polymers have recently attracted attention for their great tensile properties and good synergy with the fused deposition modelling additive manufacturing method. However, due to poor layer adhesion properties, their interlaminar fracture toughness is low. To overcome this issue, interlaminar toughening approaches inspired by Nature can be applied, exploiting the shaping freedom afforded by fused deposition modelling. Three such approaches are studied here: the side-by-side printing approach (also known as the matchstick approach), z-pinning, and layer waviness (achieved through sawtooth layers). After solving the manufacturing complications arising from the introduction of these approaches, their effectiveness in increasing the Mode I interlaminar toughness of the material is evaluated through the means of compact tension tests.

These tests reveal that z-pinning fails to meaningfully increase toughness, while the matchstick approach and especially the sawtooth layers have a beneficial effect. Z-pinning is not effective in its current form, due to the sub-optimal shape assumed by the z-pins after extrusion, which is not conducive to holding the layers together. The matchstick approach, in contrast, increases the interlaminar toughness of Vectra A950 by a factor of 1.65 for crack initiation and 2.0 for propagation. This is achieved by strengthening fiber bridging, a somewhat unpredictable toughening phenomenon naturally occurring in the material. The sawtooth layers prove to be the most effective tested toughening approach, improving the initiation toughness by a factor of 1.8 and the propagation toughness by 4.0. This quadrupling is caused by a synergy between two toughening mechanisms triggered in the material. Not only does the layers' jagged geometry stall crack growth, but it also triggers fiber bridging more reliably and postpones tearing of the fibres.

Overall, this research proves that bio-inspired toughening approaches are an excellent way to improve the interlaminar toughness of materials that are additively manufactured. It also presents a solution to the most significant drawback faced by liquid crystalline polymers, widening their uses in the aerospace industry.

Contents

1

Introduction

Fused deposition modelling (FDM) is an additive manufacturing technology during which filament is molten and extruded layer-wise into a desired shape. While initially only used by hobbyists, it is now a manufacturing method also used to produce prototypes and parts in the aerospace industry. The shaping freedom provided by FDM is best exploited by anisotropic materials such as continuous fiber-reinforced 3D-printed composites, since it allows exact alignment of the material's strongest direction with the loads experienced by a given part. However, such composites often exhibit printability issues, and the fibre enforces a limit on the achievable shapes. Composites are also hard to recycle, which is undesirable in an industry trying its best to be sustainable.

An alternative without any of those issues is a liquid crystalline polymer (LCP) known in the industry as Vectra A950. It has a unique microstructure that makes its tensile properties comparable to those of composites when additively manufactured, as can be glimpsed from Figure 1.1a. These values make the material highly lucrative for use in the aerospace field. Unfortunately, LCP also has a drawback: bad adhesion between the layers. Due to this shortcoming, parts printed from Vectra A950 have a low interlaminar fracture toughness, and are easy to delaminate. To see this, one can compare LCP with polylactic acid (PLA), a typical printing material. This comparison is visualised in Figure 1.1b. It can be seen that the area under the force-displacement curve corresponding to LCP is smaller than that of PLA. This area represents the necessary energy to fracture the material, and serves to visually display LCP's less than desirable fracture toughness.

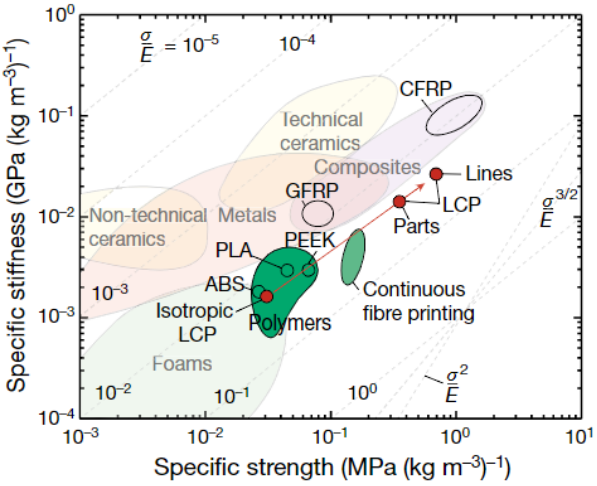

(a) Ashby chart comparing the tensile properties of thermotropic liquid crystal polymers with other engineering materials [1]. LCP parts compare favorably to conventionally produced GFRP and CFRP, an advantage over other printing materials such as PLA and ABS.

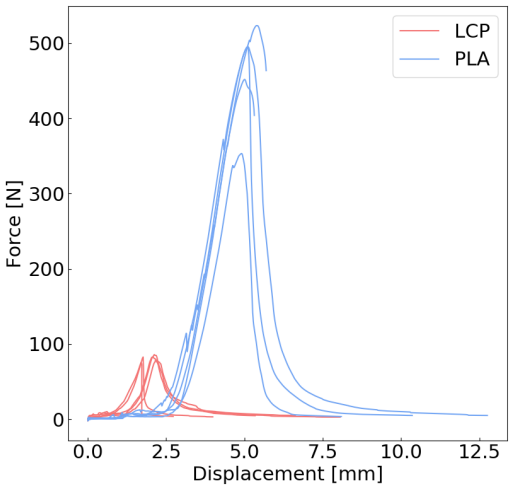

(b) Force-displacement curves of LCP and polylactic acid (PLA). PLA's superior layer adhesion grants it high fracture toughness, as can be seen from the area enclosed by its curve. LCP has bad layer adhesion, hence performs worse.

Figure 1.1: Tensile and toughness performance of LCP

Nevertheless, LCP is not the only material to exhibit this drawback. Many materials in nature have a low fracture toughness on their own, and yet are often found in biological structures with a toughness several orders of magnitude

higher. A classical example is the brittle mineral aragonite used by mussels as the building block of the tough material nacre. Another example is the wavy structure found in the dactyl club of the mantis shrimp as shown in Figure 1.2. The dactyl can repeatedly sustain impact at an acceleration of 10,400 G when the mantis shrimp strikes its prey [2]. From this it can be concluded that low fracture toughness of the base material is not an obstacle to the toughness of a structure as a whole, provided that the proper toughening approaches are applied to it.

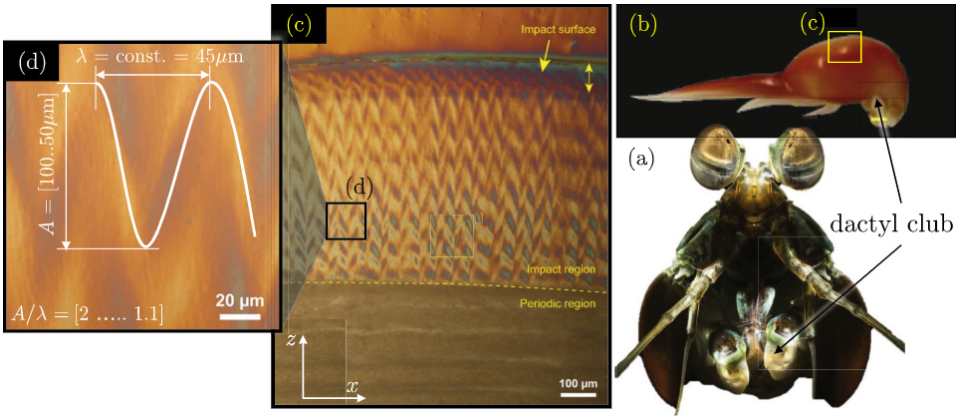

Figure 1.2: Structure exhibiting layer waviness in the dactyl club of a mantis shrimp *(Odontodactylus scyllarus)* [3]

In this project, toughening approaches inspired by nature will be applied on Vectra A950 parts produced through filament deposition modelling with the aim of improving their interlaminar toughness. Should the research prove successful, it will fully unlock the potential of LCP as a strong, stiff, tough and recyclable material to be used in the aerospace industry.

2

Literature study

Introduction

This chapter presents the goals of the research to be undertaken, as well as the state-of-the-art on topics relevant to it. It is divided in five sections. In the first, the main objective is defined. In the second, important information on the material to be used is reported. Next, the physics crucial to understanding fracture are investigated. The fourth section concerns various toughening mechanisms that have been studied before which are inspired by nature. Finally, discrete research questions are defined, and the steps necessary to answer them outlined.

2.1. Research objective

The main objective of this research project is to improve the interlaminar toughness of the promising aerospace-grade material Vectra A950 by introducing toughening structures in it during additive manufacturing. Besides from the toughening effect of the approaches employed, attention will be paid to the manufacturing complications they introduce as a secondary objective.

2.2. Liquid crystalline polymers as a printing material

The material that shall be used in this research is a type of thermotropic liquid crystalline polymer (TLCP) with the commercial name "Vectra A950". The abbreviation "LCP" is also commonly used to refer to it. This material shows promise for additive manufacturing due to a multitude of reasons, which are detailed in this section.

2.2.1. Mechanical properties

Vectra A950's strength and stiffness have been quantified by Gantenbein et al [1] and are presented in Figure 1.1a. The Ashby chart reveals that printed liquid crystal polymers (LCP) exhibit comparable specific stiffness to glass fiber reinforced polymers (GFRP) and even outmatch them in specific strength, being comparable to carbon fibre reinforced polymers (CFRP). However, CFRP still exhibit higher stiffness.

Nevertheless, this comparison is incomplete. While the LCP properties shown in Figure 1.1a are for LCP parts/lines that have been additively manufactured using the fusion deposition modelling (FDM) method, the properties for CFRP and GFRP are those of conventionally manufactured samples. Table 2.1 presents the tensile properties of FDM-printed LCP and continuous carbon fibre (CCF) reinforced FDM-printed PLA side-by-side. The subscripts "$\parallel$" and "$\perp$" denote properties parallel and perpendicular to the printed line respectively.

Table 2.1: Comparison between additively manufactured LCP and carbon fibre reinforced polylactic acid (PLA)

Material	$E_\parallel$ [GPa]	$E_\perp$ [GPa]	$\sigma_\parallel$ [MPa]	$\sigma_\perp$ [MPa]
Vectra A950 [4]	19.0	2.0	414.0	20.0
CCF+PLA [5]	8.28	-	61.4	-

This table proves that LCP is the stronger material option when one wishes to use additive manufacturing. Furthermore, CCF+PLA requires a specially designed printer nozzle and two feed lines [5], as well as coating the fibers in sizing to ensure proper fiber-matrix coupling [6]. These manufacturing complications are absent for LCP, giving that

material further advantages. The only property holding back Vectra A950 is its poor layer adhesion [1]. This property is the reason for its low fracture toughness, thus also the reason for the current research.

2.2.2. Nematic alignment

Thermotropic liquid crystalline polymers such as Vectra A950 exhibit behaviours of both a liquid and a crystalline material, with a transition triggered by a temperature change [7]. In Vectra A950, the "crystallinity" is due to the presence of nematic domains: areas in the material within which the molecules are aligned in close to parallel directions, as shown in Figure 2.1. Globally, these domains are oriented randomly, so the alignment has no effect. However, when molten Vectra A950 is subjected to extensional flow, such as in the extruder nozzle of a FDM printer, these domains align with each other, resulting in alignment on a global scale [8]. Gantenbein et al [1] report that once the material leaves the nozzle, the outside rapidly cools and solidifies, which preserves this alignment and forms a strong outer shell. On the inside of the filament, the cooling is more gradual, and thermal effects allow the domains to return to their more random alignment, reducing the strength of the core.

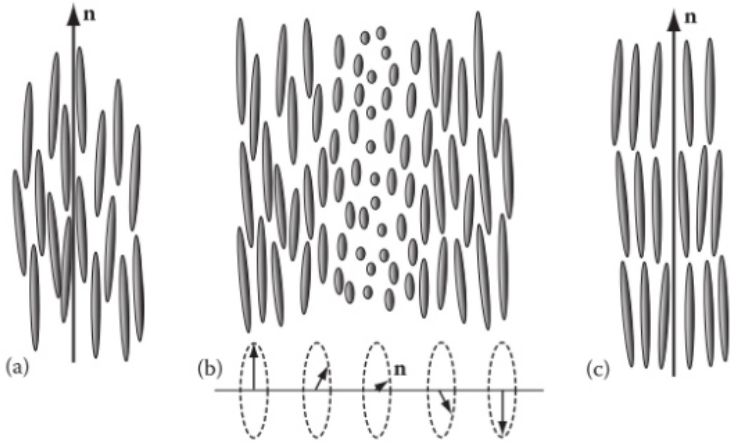

Figure 2.1: The different alignment domain types in liquid crystalline polymers [7]. Nematic domain is shown under a). Note how the different domains are all pointing in a similar direction after the application of heat and extensional flow.

This core-shell structure is of great interest in Vectra A950, as it can be affected by the printing parameters. As the layer height increases, the core grows more than the shell [1]. Naturally, since the core exhibits a lesser degree of nematic alignment compared to the skin, this results in a reduction of the the printed line's strength and stiffness, as shown in Figure 2.2a. Therefore, minimising the layer height is key to having good tensile properties.

The nozzle temperature is also a significant factor. The closer it is to the melting temperature of the polymer, the less time it takes the polymer to cool and solidify after leaving the nozzle. The preservation of nematic alignment in the outer shell is dependent on rapid cooling; if the polymer takes longer to cool, the nematic domains have more time to return to their initial random alignment. This has a negative effect on the elastic modulus and tensile strength of the printed line, as shown in Figure 2.2b.

2.3. Fracture mechanics

As the main objective of the research is to assess the fracture toughness of LCP, it is necessary to understand the fundamental principles behind crack formation. Initially, an attempt was made to find material specifically about the fracture behavior of additively manufactured Vectra A950 or a similar liquid crystal polymer. It soon became apparent that no such literature exists. As using additive manufacturing with Vectra A950 is a novel idea (pioneered by Gantenbein et al [1] in 2018), no study has been performed on this material's fracture toughness. This confirms the presence of a research gap to be filled by the current project.

In the absence of specific material on Vectra A950, fracture mechanics of fibre reinforced polymers were studied due to the abundance of literature on the subject, as well as the expected similarity between FDM-printed TLCP and CFRP/GFRP.

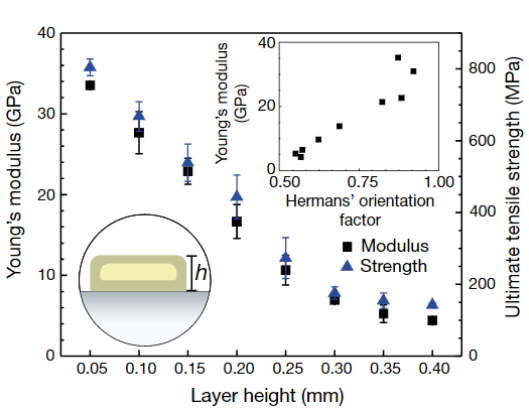

(a) Layer height effect on strength and stiffness [1]. As the layer height increases, the less aligned core comprises more of the print than the aligned skin, resulting in a drop in tensile properties.

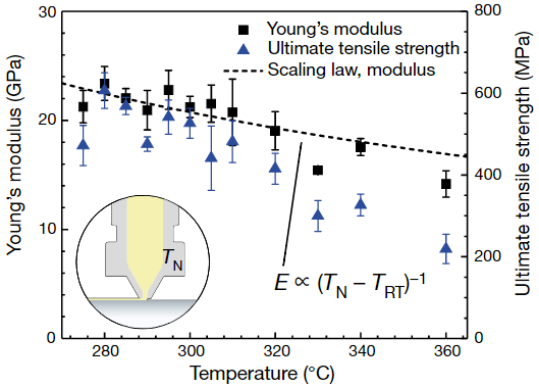

(b) Nozzle temperature effect on strength and stiffness [1]. Increasing this temperature increases the time necessary for LCP to cool and return to the crystalline phase. During this time, nematic domains fall out of alignment, which worsens tensile performance.

Figure 2.2: Effect on LCP properties due to layer height and printing temperature

2.3.1. Mode I fracture and the J-integral

The interlaminar fracture behavior of composites is defined by three modes of fracture: Mode I, Mode II and Mode III, as well as the different mixtures between these modes [9]. Mode I is known also as the tensile mode, Mode II- as the shear mode and Mode III as the transverse shear mode. As it is often the most critical failure mode in laminated solids, this research project will study Mode I fracture.

M.Laffan's work [10] presents some useful formulas used to calculate the energy released during fracture of a laminar solid, quantified by the critical strain energy release rate (SERR) G_{Ic}, a dimension-independent value. These formulas are based on linear elastic fracture mechanics (LEFM) and are widely used in the industry. However, they are also limited in scope. As pointed out by A. Brunner [9], they are defined with only unidirectional composites in mind. In cooperation with Blackman and Davies [11], Brunner goes on to state that if the crack jumps between layers, or if fiber bridging is present, any test performed under the assumption of LEFM is invalid, and the associated formulas cannot be used.

Since introducing toughening structures to LCP is the main focus of this research, it is unlikely the final product would be similar to a unidirectional composite. Furthermore, it is possible that one or more of the toughening structures causes one of the phenomena mentioned by Brunner et al [11], meaning linear elastic fracture mechanics would not apply.

To avoid these issues, one can instead use elasto-plastic fracture mechanics (EPFM), along with the J-integral method. This has already been shown by Jia and Wang [12] to be the go-to approach when evaluating fracture toughness of composites toughened by bio-inspired structures, a research case similar to the current one. Therefore, the same approach shall be applied here.

The J-integral method was first developed by Cherepanov [13] and Rice [14]. It is an integral taken over a contour that starts on one of the crack faces and ends on the other one without crossing the crack, with the integrand being the strain energy density minus the work of the traction forces. If the latter are 0, the integral becomes path independent. The integral is visualised in Figure 2.3a. Similarly to G for the LEFM case, J is a measure for the energy released during fracture, and it is independent of the sample's dimensions.

When considering Mode I fracture, the J-integral has two components. The first is the elastic one, J_{el}, which accounts for the energy necessary to initiate a crack in a given material. The second is the plastic component J_{pl}, which accounts for the energy needed to propagate the crack from initiation to final fracture [12]. These are also referred to as the initiation and propagation component, and the notations G_{init} and G_{prop} can also be used to represent them (since J is an extension of G to the elasto-plastic case).

After crack initiation, as the crack length a begins to grow, it faces increasing resistance by the material, causing the J-integral to increase [17]. This behaviour is usually recorded in the so-called $J-R$ curve, in which the J-integral is plotted against the crack length, as shown in Figure 2.3b. The J-R curve provides complete information about the

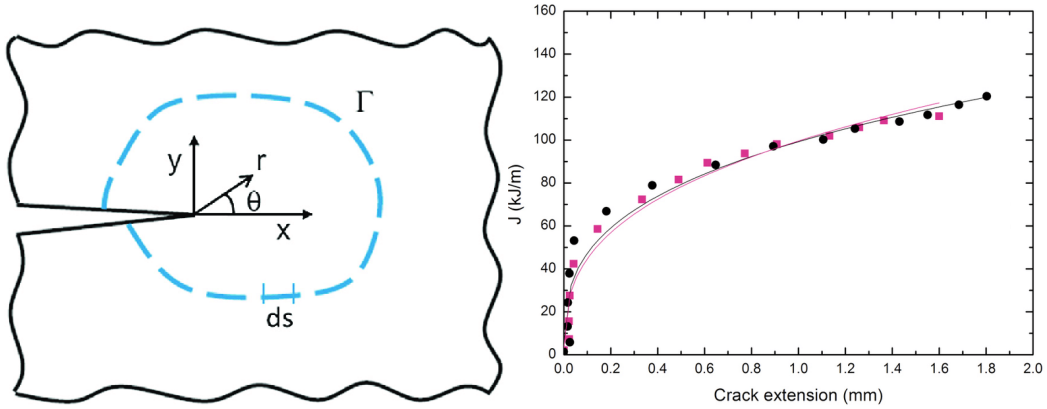

(a) The integration contour of the J-integral, with the path starting on one crack face and ending on the other [15]

(b) A typical $J-R$ curve, visualising the increasing amount of energy required for crack propagation as the crack length increases [16]

Figure 2.3: J-integral in concept and execution

fracture toughness, as one can glimpse from it both the initiation component J_{el} (which is the value J assumes at a crack length of zero) as well as the propagation value J_{pl} and how that values scales with the crack length.

2.3.2. Fracture testing procedures

The next step is to identify suitable testing methods to quantify Vectra A950's interlaminar toughness with the new toughening structures. Since no methods specific to this material exist, tests used for composites and plastics shall be considered. Of those, quasi-static tests are the most suitable, due to their simplicity and the small amount of time they require to execute.

In composites, Mode I toughness is typically tested according to the ASTM 5528 standard. It uses a double cantilever beam (DCB) specimen with glued-on testing blocks/piano hinges which are pulled apart in a tensile machine, which causes the pre-made crack at mid-thickness to propagate. The set-up is shown in Figure 2.4. The compact tension (CT) and single-edge notch bending (SENB) specimens are also commonly used, as indicated by the ASTM D5045 standard. They are presented in Figures 2.5a and 2.5b. It should be noted SENB is impractical for interlaminar tests of composites or 3D-printed samples due to its shape (layers must be parallel to the crack, making it tall, slender and hard to manufacture). Therefore, for this research, only DCB and CT shall be considered.

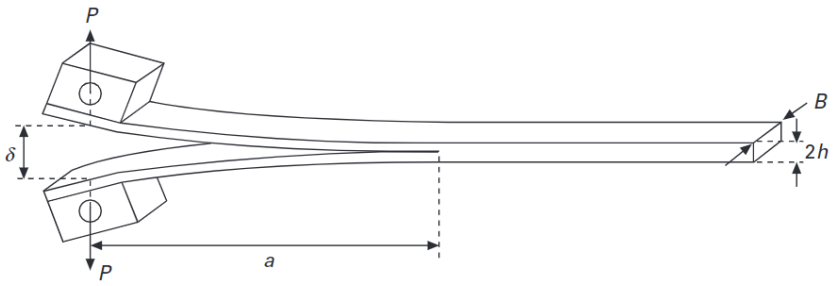

Figure 2.4: Double cantilever beam (DCB) testing set-up [10]. Loading blocks are glued to the two ends of the sample and then pulled apart, causing the starter crack created during manufacturing to propagate.

Both ASTM 5528 and ASTM D5045 are primarily intended to calculate the elastic strain energy release rate G_{init}. They can be used to obtain a $J-R$ curve as well, but in that case the more complicated compliance calibration testing procedure must be followed. It requires loading to increase and decrease repeatedly so that the sample's compliance can be measured. Furthermore, plane strain conditions must be maintained at all times. Since this complicates testing, and because it is possible to obtain the final value of the propagation energy release rate G_{prop} even under normal conditions [12], this research made the choice to use the default displacement-controlled loading procedure with a steadily increasing displacement. Therefore, the tests can be used to obtain values for the elastic and plastic strain energy release rates, but are not valid for establishing the full relationship between J and the crack length a.

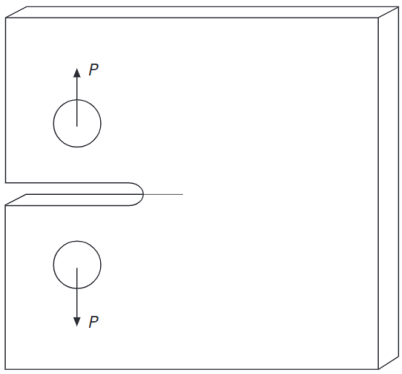

(a) Compact tension (CT) specimen [10]. Pins are inserted inside the loading holes of the sample before it is pulled apart, similar to the DCB specimen. The crack initiates and propagates from the tip of the manufactured notch.

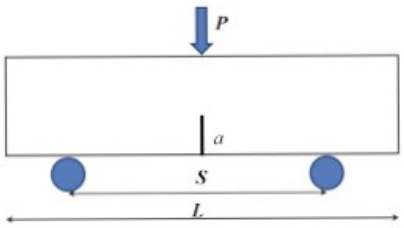

(b) Single edge notch specimen in the three-point bending loading position [18]. As the force is applied and the specimen bends downward, a crack initiates and propagates from a notch or a pre-made starter crack.

Figure 2.5: Alternatives to DCB for Mode I testing

2.4. Bio-inspired toughening

Many structures in nature exhibit high fracture toughness while being comprised of materials whose toughness on their own is one or several orders of magnitudes lower. The textbook example is nacre, or mother-of-pearl, which is remarkably tough despite brittle aragonite platelets accounting for 95% of its volume [19]. Unfortunately, the toughening approches in nacre, such as asperities and mineral bridges [20], are not easily applied to additively manufactured LCP. However, nature has many other approaches to increasing toughness. Emulating some of them is a great way to increase the interlaminar toughness.

2.4.1. Toughening in wood

Wood is a hierarchical material, with relevant structural properties on multiple scales [21]. Due to its multi-scale composition, wood exhibits multiple crack-arresting mechanisms, which result in a high fracture toughness [22]. As Vectra A950 is also a hierarchical material [1], studying wood could be a promising avenue to explore for increasing interlaminar toughness, especially since LCP can be made more wood-like through the matchstick approach, in which short lines are printed side-by-side, like the grains in wood.

Most of the toughening mechanisms in wood trigger after a crack has already initiated in the structure [23]. Therefore, they increase the propagation toughness G_{prop} more than the initiation toughness G_{init}. Chief among these mechanisms is fiber bridging. It is a process also present in composites, during which fibers are left in the wake of the crack as it propagates through the material. These fibers connect the two crack faces and take on more and more load until they tear [24]. Mirzaei et al [25] have studied this crack shielding mechanism in great detail and developed an equation that describes the effect of fiber bridging on the J-integral. It is shown in Equation 2.1.

$$J_{br}(\delta_{root}) = J_{tip} + \int_0^{\delta_{root}} \sigma(\delta) d\delta \tag{2.1}$$

Where J_{br} is the fracture toughness with the bridging accounted for and J_{tip} is the J-integral if the contour is drawn at the very tip of the crack (hence excluding the effect of fiber bridging). σ is the stress experienced by bridging fibres as a function of the crack tip opening displacement (CTOD) δ, which ranges from 0 at the crack tip to δ_{root}. This is the value at the "root" of the bridging region, as higher values cause fibres to tear and stop shielding the crack. The area between the crack tip and the root is also referred to as the process zone, as shown in Figure 2.6.

The maximal crack tip opening displacement δ_{root} has great influence over how effective fiber bridging is as a toughening mechanism, with an increase causing a corresponding increase in J_{br}. Therefore, it is not surprising that Nairn et al conclude that a higher grain length in wood corresponds to a higher toughness [26]. Since the grain is longer, so are the fibers spanning the crack, meaning that they can sustain a bigger δ_{root} before tearing.

2.4.2. Z-pinning

In composite materials, z-pins have seen success as a reinforcing element. Z-pins are thin "nails" that are driven through the layers of a composite with the help of an ultrasonic horn. According to Mouritz , these pins greatly

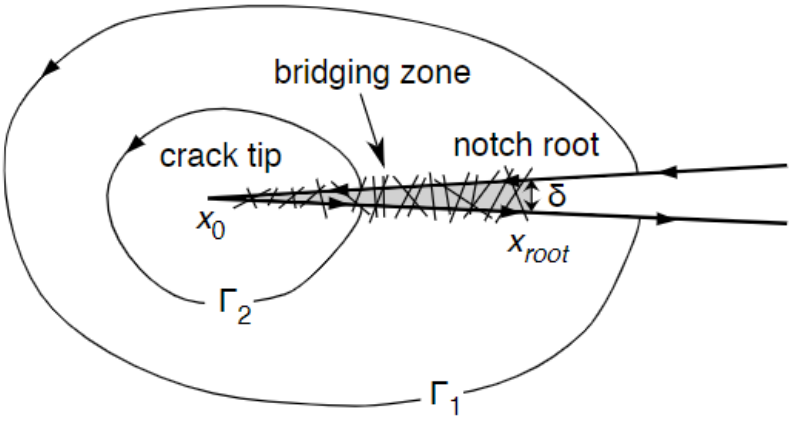

Figure 2.6: Fibre bridging zone in wood. When the crack opens, fibers are left behind. These fibers stretch more and more as the crack faces move apart, until they are loaded to the point they tear. The bridging zone moves together with the crack tip and acts to shield the crack from the load, improving fracture resistance. [26]

improve Mode I interlaminar toughness [27].

In additively manufactured samples, similar structures can be created by printing pins continuously during the manufacturing of the part itself. This is the main concept behind the work of C.Duty et al [28]. It is illustrated in Figure 2.7. The method involves purposefully leaving holes in each layer while printing, and then printing a vertical pin several layers high to fill that gap. The process is then repeated every few layers. Unlike in the case of composites, here the pins do not pass through the whole thickness, but only a few layers. Therefore, one hole contains several pins stacked vertically.

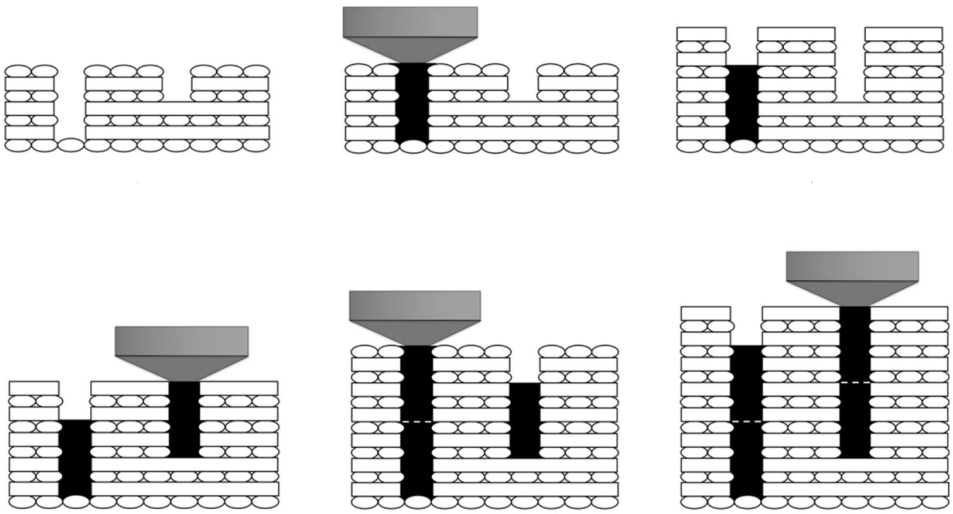

Figure 2.7: Steps in the z-pin printing process [28]. First, a hole is left in the part while printing. A few layers later, a z-pin is printed into this hole. The process repeats every few layers.

C.Duty's additive manufacturing z-pins can also be thought of as a macro-scale version of mineral bridges: vertical columns in nacre that increase its interlaminar toughness by connecting adjacent layers. Gu et al report that the presence of mineral bridges can as much as double the fracture toughness [29]. Even if z-pins achieve only a fraction of that toughening, they are still an approach worth investigating.

2.4.3. Layer waviness

Another toughening approach encountered in nacre is wavy layers. One can have either uniaxial layer waviness (waviness about only one of the print plane axes) and biaxial layer waviness (waviness about both the x- and y-axes). Biaxial waviness has been found to be more beneficial by Djumas et al [30] due to restricting displacement in all in-plane directions rather than just one. It also leads to the basic building block of the structure being an osteomorphic

block, which is a damage-resilient and interlocking shape.

Interlocking of layers is one of the main benefits of layer waviness. It causes more energy to be dissipated before fracture and inhibits delamination [31]. This is because layer waviness fracture energy is spread over a larger area, as reported by Mencattelli et al [3]. The study of nacre mimics performed by Ding et al [32] confirms this, as wavy samples were found to be 8.11 times tougher than non-wavy ones. This improvement was found to be dependent on the wavelength. The shorter the wavelength, the "wavier" the surface and thus the higher the increase in toughness.

The fact that the crack must follow the wavy layer instead of propagating along a plane also results in increased interlaminar toughness. This is due to two reasons. First, the length a crack must reach to fully fracture the sample increases, as the crack is not propagating in a straight line (the most direct path) but must follow the wavy profile. Cordisco et al [33] report that the effect of the increased length is especially notable for high amplitude, "wavier" surfaces. Second, there is the mode mixity effect reported by Zavattieri et al [34]. It is the more significant of the two effects in samples with a low amplitude. Its cause is the crack tip moving at an angle to the horizontal plane as it follows the wavy surface. Due to this, the local fracture mode at the crack tip is a mixture of Mode I and Mode II, even if the global loading conditions and sample geometry would otherwise induce Mode I. Mode II is a better fracture mode in laminar solids, with a fracture toughness up to three times higher [35]. Therefore, if fracture happens partially in Mode I and partially in Mode II, the overall result is an improvement in both initiation and propagation fracture toughness.

Nevertheless, there are also drawbacks to layer waviness. According to C.Houriet [36], wavy plies have an in-plane tensile strength equivalent to straight plies at an angle of θ to the load, where θ is the maximal angle of the waves with respect to the horizontal plane. This means that the increase in toughness comes at the cost of strength, especially for structures with high waviness. There are also the manufacturing considerations. Mencattelli et al [3] point out that structures with high waviness have very deep "valleys" which can be difficult for a print head to reach. C. Houriet adds that creating high out-of-plane waviness on a Prusa printer results in a reduction of print speed, regardless of machine settings [36]. As Vectra A950 exhibits both higher tensile strength and better layer adhesion when printed at high speeds, this lessens the benefit of waviness.

2.5. Research questions

The first and main question to be answered by this research is to what extent the introduction of a toughening approach affects the Mode I interlaminar toughness of a FDM-printed Vectra A950 sample. This question shall be answered for three toughening approaches: z-pins, layer waviness and the matchstick approach. The toughening will be quantified by comparing the toughness of five specimens toughened by a given approach with five pristine samples.

The second research question is how the introduction of a toughening approach affects the elastic modulus of FDM-printed Vectra A950, as well as its yield and ultimate stresses. This comparison shall be performed for the same toughening approaches considered in the first question, once again comparing five toughened samples with five control specimens.

Finally, the research shall consider whether or not introducing a given toughening approach makes manufacturing through FDM challenging and to what extent the manufacturing time is affected by the introduction. These questions shall be answered by tracking difficulties encountered during the manufacturing process and measuring the increase in manufacturing time caused by each toughening approach.

3

Methods

Introduction

This chapter presents the methodology behind each step in the research process, from generating sample geometries virtually before printing to post-processing of the data after testing. It is divided in five sections. First, the software and printer used to create the samples are presented. Then, the toughening approaches employed on the samples are discussed. These approaches limit the manufacturing in some ways, which are discussed in the third section. Afterwards, the procedures used to test the samples are covered. In the last section, the focus is on post-processing of the data obtained from the tests.

3.1. Slicing and printing facilities

For conventional parts, additive manufacturing is a straightforward process. First, a CAD file of the desired geometry is loaded in a special software called a *slicer*. The slicer allows the user to control important printing parameters such as infill, printing speed and printing temperature. Once those have been defined, the slicer generates a *g-code*: a series of commands for the 3D-printer. This process could not be followed in the current research, as commercially available slicers and printers do not support several cornerstone aspects of the work. A different process had to be followed instead, using a self-developed slicer and a 3D-printer modified especially for LCP research.

3.1.1. Slicing with Rhino Grasshopper

Conventional slicer software supports complicated part geometries, but is limited to simple layer geometries (flat layers, continuous lines). However, the toughening approaches listed in Chapter 2 require complex layer geometries (non-planar layers, gaps in the lines) when additively manufactured. At the same time, the part geometry of testing specimens is usually simple. Hence, available slicers are not right for the job.

The alternative is to develop a new slicer tailor-made for the requirements of the research. Though this can be done in Python, the choice was made to use Rhino Grasshopper instead. This is due to the ability to visualise each individual command of the slicer in a Rhino window with a single click. Grasshopper includes a host of useful predefined components, which enable mathematical, data-sorting, CAD and code-editing operations to be seamlessly blended in the same software. These components can be connected by dragging and dropping links between them. This forms a string of operations to be performed sequentially, as shown in Figure 3.1. With Grasshopper, the desired geometry can be generated in the same software later used to slice it, an advantage over conventional slicers, which can only generate simple preset shapes (cubes, pyramids, cylinders, spheres etc).

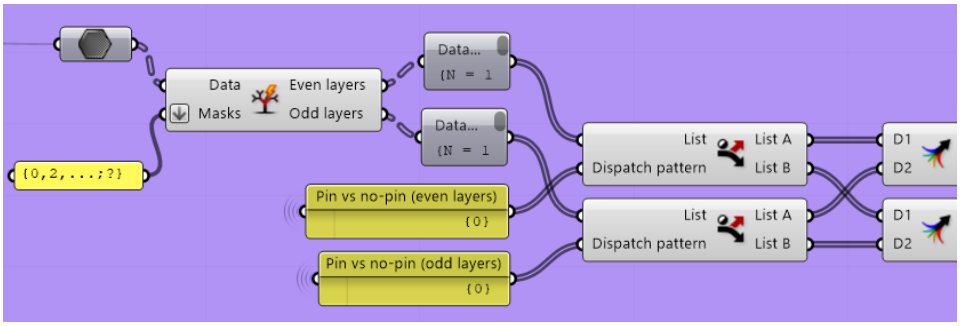

Figure 3.1: An example of Grasshopper components in a sequence, in this case a filter that splits the print lines in a sample based on layer and whether they contain pins.

The sequence of actions in the Grasshopper slicer is broadly as follows. First, the geometries of the testing specimens (tensile and compact tension) are generated based on dimensions input by the user. Then, the user chooses one of these specimens to continue with. Also selected at this stage are the toughening approach to be applied (if any), along with the value for the control parameter of that approach. The software then transforms the solid defined in the first stage into a collection of lines for printing, applying the chosen toughening approach where required. The start- and endpoints of each line are obtained, and the points for the sample brim are added to the data (if the option to have a brim is enabled). This point cloud is copied several times if the user selects the option to print multiple samples. Finally, the coordinates of each point are taken, transformed into g-code commands and saved as a text file. Briefly before this, a set of commands used to start and end the printing process are appended to the start and end of the file, respectively.

3.1.2. Printing facility

LCP parts have been manufactured using fused filament fabrication (FFF) 3D-printers in the past [1], so this is also the technology chosen for this research. However, one cannot just take any FFF printer, load LCP filament in it and start printing. Vectra A950 must be printed at higher nozzle temperatures than other filaments (usually 300°*C*), so a brass nozzle must be used instead of a steel one, and the firmware must be adapted to allow printing at such temperatures. Therefore, a Prusa i3 MK3S+ printer with these modifications is the one exclusively used in this project for printing with LCP.

3.2. Bio-inspired toughening approaches

In this research, three approaches will be considered for increasing the Mode I fracture toughness of Vectra A950. These are the matchstick approach, z-pinning and sawtooth layers. They all take advantage of the shaping freedom afforded by additive manufacturing in their own unique fashion. Each of the approaches also has a control parameter- a key variable that controls how "strongly" the approach is applied. By varying that parameter and assessing the effect on fracture toughness, a relationship between the two can be established. To this end, three values of each control parameter shall be tested, with five samples per value to permit statistical evaluation. Samples with continuous UD lines without any toughening approaches applied will also be printed as control specimens. A visual representation of all the sample types is shown in Figure 3.2.

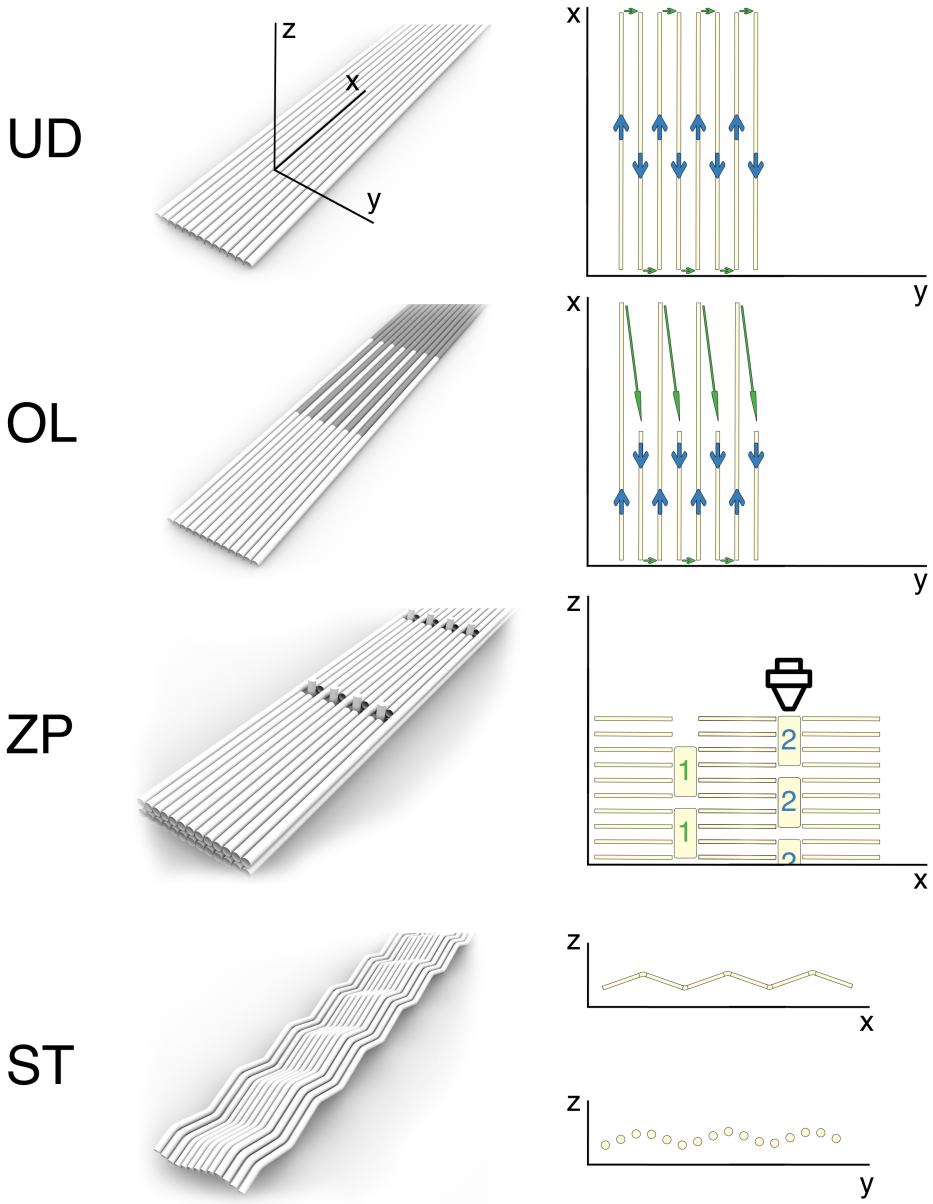

Figure 3.2: Visualisation of the control specimens (*UD*), as well as the three toughening approaches: matchstick approach (*OL*), z-pinning (*ZP*) and sawtooth layers (*ST*). Also shown on the right are the motions done by the printer to create these geometries.

3.2.1. Matchstick approach

Being the only fully planar toughening approach among the three, the matchstick approach is also the easiest to execute. It consists in printing short lines ("matchsticks") side-by-side to take advantage of LCP's better adhesion while it is hot [1]. In the context of the samples that will be printed in this research (which have rectangular layers and 100% infill), it means switching from the *UD* case of uninterrupted long lines that span the whole sample length to shorter matchsticks that are printed side-by-side. These matchsticks are not printed exactly aligned, but so that each one is offset 50% of its length with respect to the ones adjacent to it, as shown in Figure 3.3. This leaves 50% of the matchstick length as an overlap between adjacent lines. The length of this overlap, or the overlap length (*OL*) is the selected control parameter for the matchstick approach. Samples with three different values of overlap length will be tested, namely overlap 5 mm (*OL*5 mm), overlap 10 mm (*OL*10 mm) and overlap 20 mm (*OL*20 mm).

When *OL* is increased, the matchstick length is increased proportionally, maintaining a 50% overlap ratio at all times. This is done to offset the ends of adjacent matchsticks as much as possible from one another. Having them closer would make it easier for cracks to propagate between rows of matchsticks, creating a structural weakness.

It should be noted that unlike the other two approaches, the matchstick approach does not have a direct equivalent in the literature studied. It is completely untested in the sphere of fracture toughness. Even though it brings LCP closer to wood in structure, it is not certain that implementing it will yield positive results. Nevertheless, it is a novel approach to 3D printing worth studying, and it would be promising if it also provides a toughening effect.

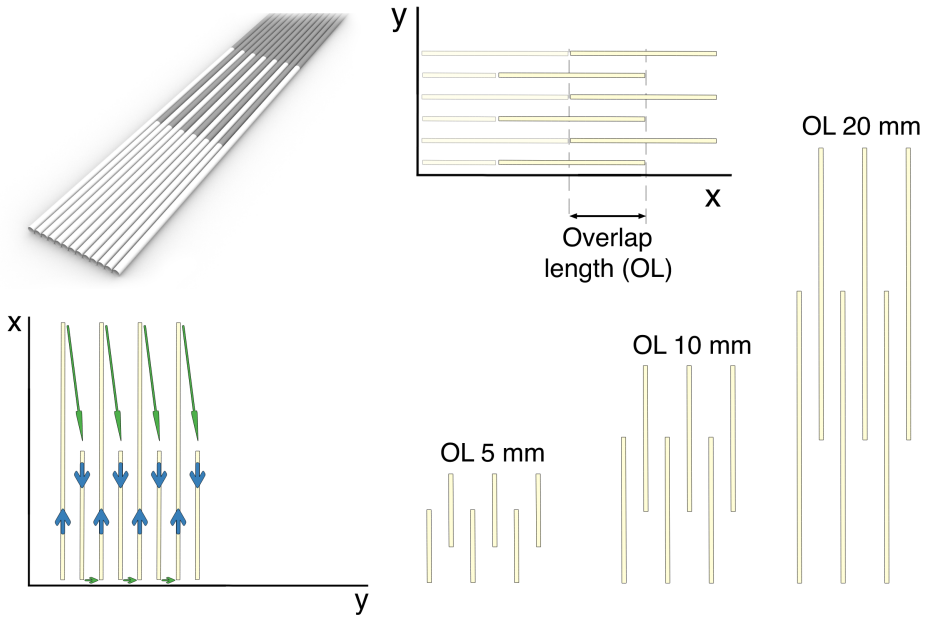

Figure 3.3: The matchstick approach in detail. The brick-like arrangement of parallel matchsticks is meant to increase the path a crack must travel to separate them, potentially increasing the toughness.

3.2.2. Z-pinning

Unlike the matchstick approach, z-pins have been widely used for toughening. They are perhaps the most straightforward way to improve Mode I toughness, using reinforcements in the z-direction to hold the layers together and postpone their separation. Its implementation in the current research is shown in Figure 3.4. The figure's bottom-most row shows the three-step process of creating the z-pinned specimens. First, continuous lines are printed where no z-pins will be placed. "Dashed" lines are then printed between them, leaving gaps into which the z-pins will go later. This completes one layer. Several layers are printed by repeating these two steps, until the depth of the gaps becomes equal to the target z-pin height. Finally, before starting the next layer, the nozzle moves to the locations of the gaps and extrudes without moving, filling the gaps and creating z-pins. The whole three-step process then gets repeated. At the end, all gaps are filled by z-pins stacked on top of each other.

It should be noted that during the third step of the process, z-pins are not printed in all of the gaps, but only in half of them in a chessboard arrangement (marked with "1" in the figure). Then, a number of layers later equal to half the z-pin height, z-pins are extruded in the other half of the gaps (marked with "2"). This is done to stagger adjacent z-pins in the z-direction, so that the ends of z-pins are not all on the same layers. Such layers would not be reinforced by the z-pins, which is undesirable.

The control parameter for z-pinning is the z-pin density, or the ratio of z-pins penetrating a given layer to that layer's geometrical area. By increasing the amount of pins in a layer, the density also rises. It can be straightforwardly calculated as:

$$\rho_{ZP} = \frac{N_{pins}}{w_{layer} * L_{layer}} \tag{3.1}$$

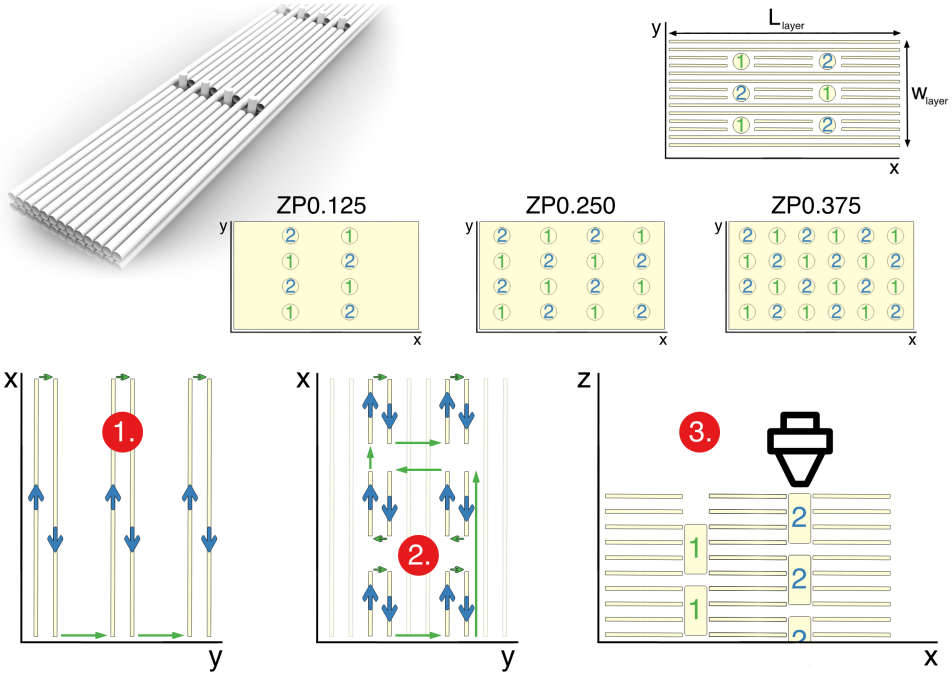

Figure 3.4: Z-pinning in detail. Each layer contains both continuous lines and "dashed" lines with gaps in them. Every few layers, z-pins are extruded into these gaps. Z-pins are staggered in z to avoid end alignment.

Where ρ_{ZP} is the z-pin density, N_{pins} is the number of pins in a given layer, and w_{layer} and L_{layer} are the width and length of the same layer. For the fracture specimens, this layer is the one right at the crack tip, as that is the location at which fracture occurs. For the tensile specimens, the exact layer does not matter, as all layers have the same width, length and number of z-pins. Samples with three different densities will be produced and tested: samples with a density of 0.125 pin/mm^2 (ZP0.125), ones with a density of 0.25 pin/mm^2 (ZP0.250) and ones with a density of 0.375 pin/mm^2 (ZP0.375).

3.2.3. Sawtooth layers

As mentioned in Chapter 2, using sinusoidal wavy layers instead of flat ones can be highly beneficial to toughness. Therefore, this research initially had the goal to use that same strategy on LCP and evaluate its toughening effect. To create a sinusoidal line with a 3D-printer, there are two options. One is to split it into many short linear segments printed in a sequence. This is not practical, as having so many commands to print a single line causes the printer to move at a slower speed than the one set in the Grasshopper slicer. This introduces another variable, precluding the effect of layer waviness from being evaluated on its own. The second option is using the *G*4 printing command to represent the sinusoidal line as a spline, which takes only one command. However, this command is relatively new, and the firmware of 'Moebius', the printer used for the research, did not have it implemented. As updating firmware is a complicated procedure, the decision was made to adapt the layer geometry to the available commands.

This adaptation involves the use of "sawtooth" wavy layers instead of sinusoidal ones. A "sawtooth" line is an approximation of a sine wave that consists of tilted linear segments (printed with the standard *G*1 printing command) joined at their ends by circular arcs (printed with the clockwise and counter-clockwise arc commands *G*2 and *G*3). Figure 3.5 reveals that the final shape of the layers is not far off from the structures studied in literature, such as Mencatelli and Pinho's herringbone bisinusoidal layers [3], making this adaptation a good compromise.

The control parameter chosen for the sawtooth layers is the layer sharpness angle ϕ. For a sawtooth line, it is defined as the lesser of the two angles between a tilted linear segment from the line and an imaginary horizontal line bisecting the sawtooth line, as shown in Figure 3.5. Since the sawtooth layers are wavy in two planes (zx and zy), it should be noted that the same sharpness angle is used for both planes in all samples. ϕ can also be geometrically calculated from more typical wave parameters, which is shown in Equation 3.2.

$$\phi = atan\left(\frac{A}{\lambda/4}\right) \tag{3.2}$$

Where ϕ is the layer sharpness angle and A and λ are the amplitude and wavelength of the pattern, respectively. Samples with three values of sharpness angles will be produced and tested. The selected sharpness angles are 10° (ST10°), 15° (ST15°) and 20° (ST20°). However, it should be noted that although sharpness can be increased by either increasing the amplitude or decreasing the wavelength, in this research project only amplitude was increased, with the wavelength kept always equal to the sample width. The reasoning behind this is that as the wavelength reduces, more linear segments and circular arcs are necessary to create one printing line. This again introduces printing speed as a variable, defeating the main purpose of using the sawtooth approach.

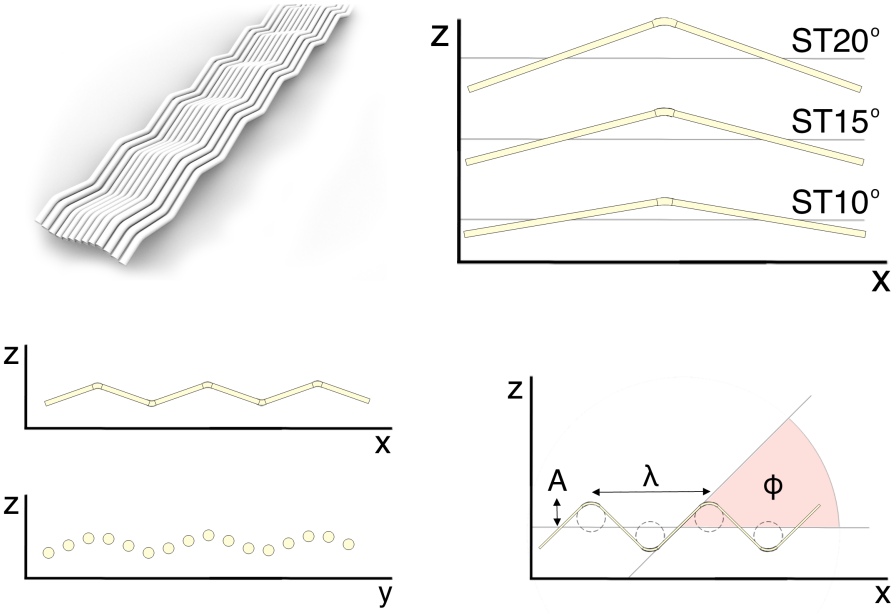

Figure 3.5: Sawtooth layers in detail. Note that the change in sharpness angle ϕ is achieved only through increasing the amplitude A.

While literature indicates that increasing wave sharpness angle has a big benefit to toughness, this research chose to limit itself to samples with up to 20° degrees of waviness. This is due to the interaction between sawtooth layers and sample cutouts during printing. The issue is visualised in Figure 3.6. It is caused by the necessity for support structures, lines printed to hold up a part of the sample that cannot stand on its own. They are necessary in cutouts that span the z-direction. Without them, lines printed above the empty space collapse, and the print fails.

All support structures in a cut-out must be printed after all lines below the cutout have been printed (so that the printhead does not smash the support by trying to print under it) and before any lines above the cutout have been printed (as without support they will just collapse as mentioned). With normal, flat layers, this is not an issue at all, and support is printed in parallel. For sawtooth layers, however, a problem arises at high amplitude. In contrast to flat layers, the distance that a layer spans in the z-direction is equal not to the layer height, but to twice the amplitude. When this span is bigger than the thickness of the cutout (in the z-direction), eventually there will come a point during printing when the printhead is extruding material above and below the cutout in the same layer. Due to this, it is impossible to print support material without running into at least one of the aforementioned issues. For the current research, the cutout height is such that the highest achievable angle is 20°.

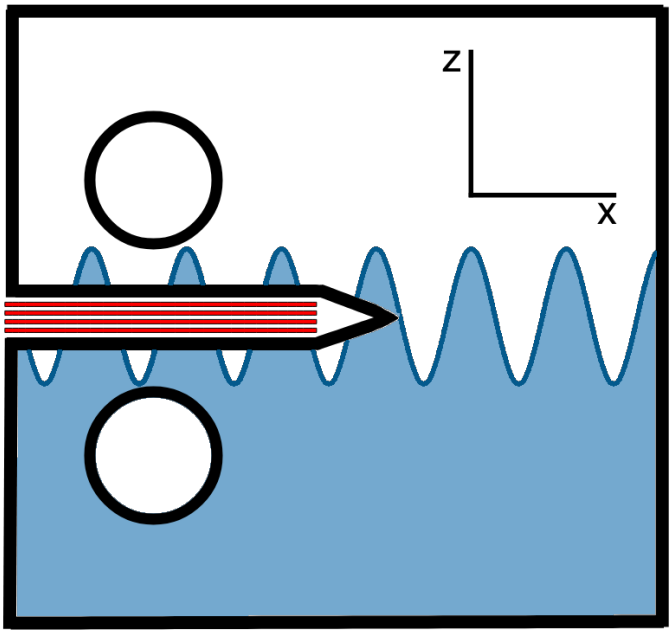

Figure 3.6: A sample where printing support is impossible due to a sawtooth layer that has lines both above and below the cutout

3.3. Manufacturing procedures and challenges

Additive manufacturing is a process with many parameters, and each of those can affect the performance of the created sample, or even whether the sample can be printed in the first place. The use of Vectra A950 as the printing material introduces further factors that need consideration, and so do the toughening approaches. Several months of the research process were dedicated to eliminating issues arising from one of these sources.

3.3.1. Basic process parameters

LCP lines are extruded at a line width of 0.4 mm and a layer height of 0.1 mm. This height is chosen to ensure an optimal skin/core ratio in the material, which results in better tensile properties, as indicated in the work of Gantenbein et al [1]. The bed temperature while printing is set to 90 °C for a better adhesion of the material. However, LCP can still easily detach from the bed, especially if the part is more bulky. For this reason, before printing, the bed is also sprayed with Dimafix adhesive spray for better adhesion. The nozzle temperature is set to 300 °C for some samples and 330 °C for others, for reasons explained in the following subsection.

3.3.2. Material manufacturing challenges

The first issues that need to be tackled when additively manufacturing Vectra A950 are due to the material itself. Unlike PLA, the predominantly used material in fused filament fabrication, Vectra has issues sticking to the printing bed for the full duration of the printing process. The sample can curve upwards due to different temperatures at its top and bottom parts, detach from the print bed and cause print failure. A "pyramid brim" is applied to eliminate this issue. It consists of a wide first layer brim, with narrower and narrower secondary brims following in the next few layers. This novel brim reliably prevents detachment of LCP from the build plate.

Nevertheless, LCP's adhesion is not only bad between the sample and the printing bed, but between the layers themselves. This issue manifests in bulky samples which have a big height (i.e. a large amount of layers when sliced). During printing, such samples eventually reach a point where the bottom layers are kept warm by the bed and the top layers are kept warm by the printhead, while the layers in the middle, far away from either heat source, cool down to ambient temperature. This temperature differential induces loads within the samples, and with LCP's poor layer adhesion, those loads are enough to cause a crack to appear in the sample, as shown in Figure 3.7.
An increase in the nozzle temperature from 300 °C to 330 °C was initially believed to solve this issue. This change did cause bulky samples to stop exhibiting visible cracks, which allowed fifty of them to be printed. However, during testing five of those samples cracked at a location that does not make sense given the sample's geometry. This indicates

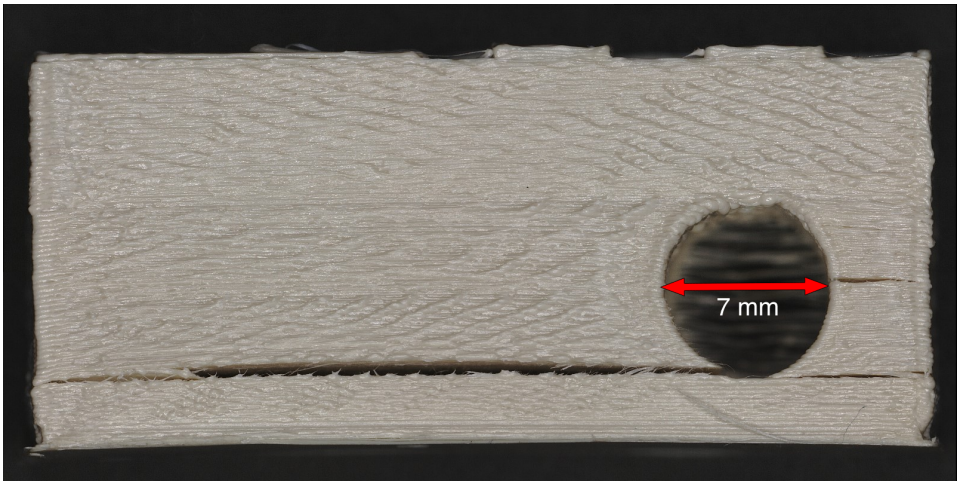

Figure 3.7: Inter-sample cracks in a tall and bulky sample, caused by the differing temperatures in the sample. Sites near holes are especially conducive to the appearance of such cracks.

the presence of a microcrack at that location which escaped notice during the visual inspection before the test. From this it can be concluded that increasing the nozzle temperature does not eliminate this issue, but merely lessens it. Furthermore, for even taller specimens, this temperature increase may prove insufficient. Therefore, inter-layer cracking in LCP parts remains an issue without a solution.

3.3.3. Z-pin manufacturing challenges

Other limitations encountered during manufacturing stem from the toughening approaches used. One such limitation has to do with the shape assumed by the z-pins during printing. The expectation is that z-pins would have a more or less cylindrical shape, like the one in Figure 3.4, and stack into a monolithic column. To verify that, the cross-section of the z-pinned samples was studied at the location of a row of z-pins. This is shown in Figure 3.8.

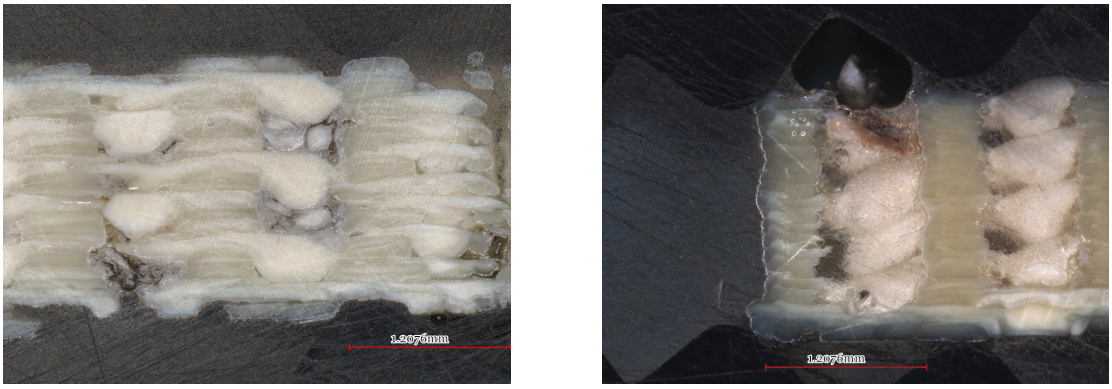

(a) 6-layer z-pins

(b) 4-layer z-pins

Figure 3.8: Microscope images of the z-pinned samples' cross-sections. The z-pins assume a "stack of drops" shape instead of a cylindrical one, and seem to have trouble penetrating more than four layers.

The first (experimental) series of z-pin samples printed had a target z-pin height of six layers (or 0.6 mm). However, as it can be seen from Figure 3.8a, the material extruded in the gaps could not penetrate all the way, leaving the bottom third of the space unfilled. To solve this issue, the next series of z-pin samples (the one that was used for testing later) used a z-pin height of four layers. Figure 3.8b reveals that pins now do reach the bottom of their gap and touch the pin underneath. Nevertheless, even then the z-pins are not cylindrical in shape and do not connect into a singular rod. Instead, they exhibit drop-like shapes and are haphazardly stacked on top of each other. It can also be seen that there is still unfilled space in the gaps.Overall, this is a very different shape from the z-pins studied in literature.

3.3.4. Sawtooth layers manufacturing challenges

Implementing sawtooth layers into 3D-printing also comes with a slew of complications. First of those is the fact that the layers are non-planar, and hence cannot be printed on a flat printing bed without collapsing. This issue can be solved through "amplitude ramping". This method involves starting with a flat layer first, then printing a sawtooth layer with a very small amplitude on top of it. Since the amplitude is so small, the layer is properly supported by the layer underneath. In the next layer, the amplitude is increased slightly. This is repeated again and again in subsequent layers, until the amplitude finally "ramps up" to the value that gives the desired wave sharpness angle ϕ. These ramp-up layers therefore provide a gradual transition between flat and sawtooth layers. Depending on whether a sample must be fully comprised of sawtooth layers or not, the ramp-up layers can either be part of the sample itself (for the latter) or form a sacrificial platform, which is discarded after the real sample gets printed on top of it.

If these layers are integrated into the sample, the change of amplitude per ramp-up layer, or ΔA, becomes a parameter of interest. If ΔA is low, then the transition from flat to sawtooth is more gradual. However, it also takes more layers to complete, which becomes a problem for thin samples with higher sharpness angles, hence higher final amplitudes. The solution is to increase ΔA. This should nonetheless be done carefully. Figure 3.9 reveals that when amplitude ramping is done over too few layers, with a big amplitude jump between layers, voids appear in the sample at the location of the sawtooth pattern's peak and valleys. These voids weaken the structure and are to be avoided. To this end, a good ΔA value must be found for each layer sharpness angle, one that gives amplitude ramping in as low a number of layers as possible without causing voids. In this project, such good values were found through trial-and-error.

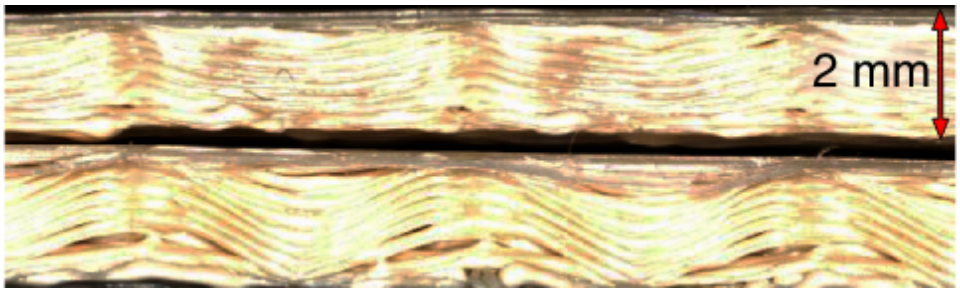

Figure 3.9: A sample with too high amplutide change ΔA (bottom sample) versus a sample with the correct ΔA (top sample). Voids are visible in the sample where amplitude ramping is done too fast.

3.3.5. Manufacturing times

Besides from introducing some complications to the additive manufacturing process, the toughening approaches employed also have an effect on the time it takes for one sample to be completed. In order to quantify that effect, the time required to print one layer of material was measured with a stopwatch for each of the printed sample types. The layer had the same dimensions in every case. The results of these measurements are shown in Table 3.1.

Table 3.1: Layer printing times of all sample types, compared to the control (UD) case

Sample Type	Time to print one layer (s)	Sample Type	Time to print one layer (s)
UD	33.9	ZP0.250	53.9
OL5	58.2	ZP0.375	60.8
OL10	45.1	ST10°	64.5
OL20	47.3	ST15°	68.9
ZP0.125	47.0	ST20°	75.6

3.4. Testing the samples

The primary goal of this project is to establish the effect of the selected three toughening approaches on the Mode I fracture toughness of LCP. Therefore, tests to quantify this parameter must be performed. However, it is also beneficial to be aware of the effect the approaches have on the material's tensile properties: yield strength, failure strength and elastic modulus. This is because good toughness properties often come at the cost of bad tensile ones. One has to be aware of both sides of this trade-off, hence tensile tests should be performed alongside fracture ones.

3.4.1. Sample types

Both tensile and fracture testing are performed according to ASTM standards. For the tensile tests, the standard D3039 is used, which covers tensile testing of polymer matrix composites. Given that Vectra A950 has shown similar properties to such materials in prior research [1], the use of this standard is justifiable. Per D3039, the tensile test specimen has the shape of a simple rectangular prism. The dimensions chosen are 110 x 5 x 2 mm. Before testing, sanded GFRP beveled tabs are glued to both ends of the specimen using DP 160 (3M) adhesive for a better grip during testing. The gage length is equal to 65 mm.

For the fracture testing, two different sample types were considered. The first is a double cantilever beam (DCB) specimen, as recommended in ASTM D5528 for use in composites. The second is the compact tension (CT) specimen recommended for plastics in D5045.

The former were initially given preference due to their simpler geometry. However, creating the sharp starter crack required by the standard proved challenging. This process is easy in composites, where it is only necessary to insert a teflon sheet during lay-up to prevent adjacent layers from sticking together. In additive manufacturing, one can similarly pause the printing mid-way, add teflon tape and then resume, but the sample becomes unusable. This is because any LCP printed on top of the teflon cannot adhere to the layer underneath, causing the lines above the sheet to curve up slightly. Furthermore, the nozzle causes the sheet to wrinkle as it passes over. These two factors cause ridge-like defects that propagate into the layers further up, as shown in Figure 3.10a. Since one of the requirements for a DCB sample to provide valid data is complete symmetry on both sides of the crack plane, an asymmetric defect like this one makes the sample unfit for use. To eliminate this defect, the teflon tape must be pulled taut to prevent wrinkles and must be sprayed with the same adhesive as the bed to prevent curving. However, this makes the tape impossible to remove from the finished sample, which is again against the requirements of the standard.

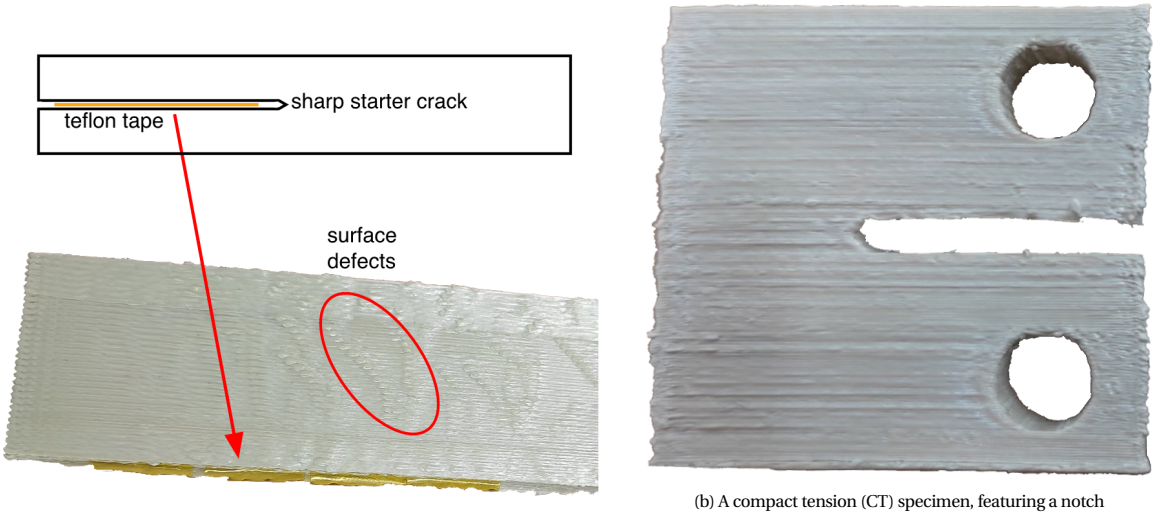

(a) Top surface ridges in the double cantilever beam (DCB) specimen caused by the teflon tape added at mid-thickness to create the starter crack.

(b) A compact tension (CT) specimen, featuring a notch instead of a starter crack. Holes for the loading pins are integrated into the sample.

Figure 3.10: The two fracture testing specimen types

Given the issues encountered with the manufacturing of the DCB specimen, the compact tension (CT) one seems a more reasonable alternative. Its geometry is shown in Figure 3.10b. Instead of having a thin starter crack which requires a film insert, the CT specimen has a wide notch which can be easily created with printing, though support material is required. This notch ends in a triangular tip, which is further sharpened with a razor to create the starter crack. Besides from avoiding the film insert, another benefit of the CT sample is the integration of holes for the loading pins into the sample itself. In contrast, DCB samples require steel blocks or piano hinges with holes to be glued to the specimens to allow connection to the testing machine. The adhesive between the samples and the blocks/hinges represents another potential point of failure which is absent in the CT sample. Due to these advantages, this research chose to use the CT sample to determine Mode I fracture toughness instead of the commonly used DCB one.

The chosen dimensions for the sample are shown in Figure 3.11. This research chose to use relatively small samples to reduce the manufacturing time. It is not a problem to manufacture bigger or smaller samples, if desired, but this

change should be done proportionally, i.e. all dimensions should be multiplied by the same factor. This is because the ratios between the dimensions is dictated by the ASTM standard with the goal of assuring plane strain conditions during testing, without which the test is considered invalid. The one exception is the sample width, which is allowed to vary between 1/5th (as in this research) and 2/5ths of the sample length. The choice in this research to use a thinner sample is due to the cracking issues mentioned in Subsection 3.3.2. The wider and bulkier the samples, the more prevalent the cracking; specimens with a width of 14 mm were manufactured and found to visibly crack during production even at the high nozzle temperature of 340 °C. Hence, a thinner sample is preferable.

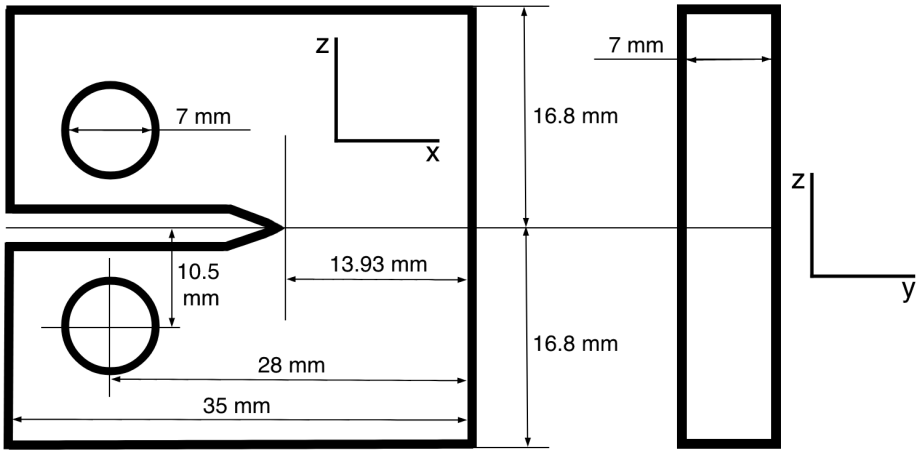

Figure 3.11: Dimensions of the CT specimen

3.4.2. Testing procedures

For both the tensile tests and the fracture ones, use is made of a Zwick 10 kN tensile testing machine, with a 1kN load cell to track the loads experienced during testing. Both the fracture and the tensile tests are displacement-controlled. The two different tests also require different setups, which are shown in Figure 3.12.

For the tensile test, hydraulic grips are used to securely clamp the sample. For the fracture test, fixtures with holes at the end are used. Normally, these holes would be aligned with the holes in the CT sample and a bolt would be driven through them for load transfer. However, the fixtures available for this research turned out to be quite big, causing the upper and lower fixture to touch when connected to the sample in this way. This is undesirable, as if something goes wrong and the lower end of the Zwick machine moves up instead of down, the lower fixture will instantly knock into the upper one, hitting the load cell at its base and damaging it. To avoid such scenarios, additional extender brackets with holes at each end were printed. These brackets are connected to the fixtures on the one end and the sample on the other end. This complicates the setup somewhat (now there are four bolts instead of two), but it is needed to minimise the chance of damage occurring to the machine.

During testing, data can be tracked in two ways. The first one is the standard load-displacement data from the machine. The second one is to employ digital image correlation (DIC). To use this method, one must apply a speckle pattern to one surface of the sample (visible on the CT specimen in Figure 3.12). The motions of the pattern are then tracked by a camera during testing. DIC was used on all of the CT specimens to record the strain field around the crack and its development as the crack progresses. For tensile tests, DIC was only used in some cases, when more data was needed to explain an interesting behaviour observed in the force-displacement curve obtained from the basic data.

After each test, the sample is taken out of the machine and each part of it is labeled with a unique identifier which was also used to mark the data obtained from that sample during the test. In that way, the destroyed samples can later be connected to the data obtained during the test, which proves useful for post-processing.

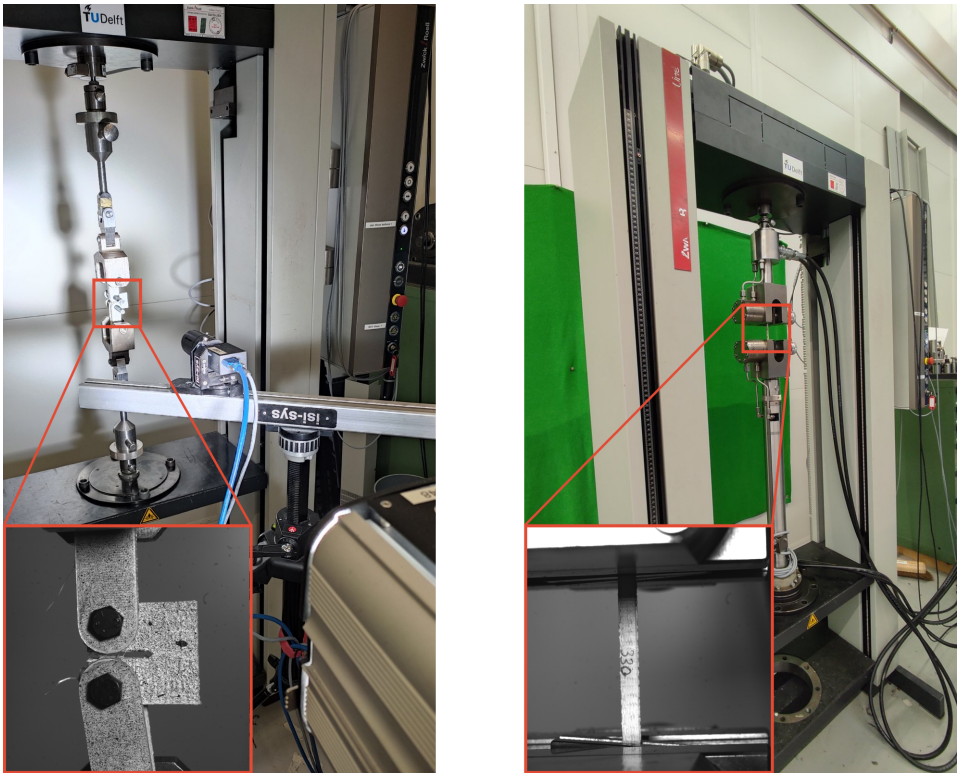

Figure 3.12: Testing setups for the fracture (left) and tensile (right) tests. The same Zwick 10 kN machine is used for both types of tests. The only difference is the use of hydraulic grip fixtures for the tensile tests and bolt-hole fixtures for the fracture ones.

3.5. Post-processing

Data directly obtained from testing, such as force-displacement curves and DIC images, can be useful for drawing qualitative conclusions about the effects of the different toughening approaches on the material properties of LCP. However, to properly quantify the effects of the toughening approaches, post-processing is required.

3.5.1. Fracture surface microscopy

For the fracture specimens, data from DIC and the testing machine is insufficient to draw all possible conclusions about toughness. Analysing the fracture surfaces of the samples can lend valuable insight into why a given specimen behaves a certain way. In this research, the fracture surface of each sample was analysed using a VR-5100 Keyence optical microscope. It was used not only to take photographs of the fracture surfaces, but also to create detailed height maps.

From the height maps, the surface-average surface roughness S_a is obtained, a useful parameter for surface analysis. It is, in essence, the average of the deviation along the z-axis of each point on the fracture surface, using as a reference a plane corresponding to a perfectly flat surface. The exact formula to calculate it is shown in Equation 3.3.

$$S_a = \frac{1}{S}\iint_S |z(x,y)|dxdy \tag{3.3}$$

Where S is the geometrical area of the fracture surface and $|z(x,y)|$ is the modulus of the z-axis deviation in a given point with coordinates x and y. The formula reveals that S_a can be affected not only by random roughness of the surface created during testing, but also by any non-planar features added to the layers by design, as is the case with sawtooth layers. However, in some cases one might want to assess only the effect of random roughness, in which case the sawtooth layer influence becomes undesirable. This problem can be solved by simply using a perfect bisinusoidal surface instead of a flat plane as the reference surface from which deviation along z is measured. This new parameter is called S_{acorr}, or corrected surface-average surface roughness. The formula to calculate it is shown in Equation 3.4.

$$S_{acorr} = S_a - \frac{1}{S}\iint_S |sin(x)sin(y)|dxdy \tag{3.4}$$

3.5.2. Processing the data

For processing and refining of the raw data from the tests, a code written in Python is used, due to the increased flexibility over a conventional tool like Excel. Since the tensile test data and the fracture test data require different analysis, two different tools were developed.

Tensile data analysis

Before analysis can begin, the data must be properly formatted. Formatting has several steps. First, a cut-off criteria is applied: if there is a force drop of 50 N or more between two data points, the data is truncated. This is done because such a significant load drop signifies that the tensile specimen has already failed, even if the test continued afterward. Next, a Savitzky-Golay filter is applied to the data to smoothen it, since inspection of the force-displacement curve showed it to exhibit a lot of random noise. Finally, the data is adjusted to always start at 0 N by shifting the force-displacement curve up. This is done to eliminate the influence of pre-loading (random negative load induced in the specimen while it is mounted in the fixture). This completes the data formatting for most samples.

In the next step of the code, the slope and curvature of the force-displacement curve are calculated using centered difference numerical differentiation. The exact formulas are shown in Equation 3.5.

$$F'(i) = \frac{F(i+n) - F(i-n)}{2[u(i+n) - u(i-n)]} \quad ; \quad F"(i) = \frac{F(i+n) - 2F(i) + F(i-n)}{[u(i+n) - u(i-n)]^2} \tag{3.5}$$

Where F is the force experienced by the samples during the test and u is the displacement. n is the stepsize for the method, which was chosen to be 20 data points. This means that in order to calculate the slope ($F'(i)$) and curvature ($F"(i)$) in a given data point, one uses the data for that point, as well as the data from 20 data points earlier and later.

In some of the specimens, the previously enforced 50 N load drop criteria proves insufficient to truncate the irrelevant part of the force-displacement curve, as the curve after the maximum load experiences a more gradual decline, rather than a sharp drop. For these specimens, a second truncating criteria is enforced, trimming the curve after the slope F' reaches a value smaller than - 50 (signifying a dropping $F-u$ curve).

Next, the minimum of the curvature over the whole curve is obtained. This most often corresponds to the moment of yielding, the point where the slope shows the most dramatic reduction. That is not always the case: some samples can exhibit brittle behavior until right before fracture, in which case that is the point that will be picked up by the algorithm. Nevertheless, that in itself is telling and allows the user to identify which samples behave more brittle and which do not.

The final step in the algorithm is to normalise the data by moving from force-displacement to stress-strain analysis (σ - ϵ). Stress is calculated by dividing the force by the cross-sectional area of each specimen (measured before testing). The displacement is divided by the gage length to obtain the strain. Now σ - ϵ curves can be plotted, and the yield and ultimate stress can be calculated. The former is calculated by simply taking the maximum, while the latter is the stress corresponding to the previously found yield point. Lastly, the elastic modulus is calculated by finding the slope of a segment of the stress-strain curve before the yield point.

Toughness data analysis

After the force and displacement data from the fracture tests gets imported into the code, the analysis takes place in two broad stages. These are the initiation and the propagation stage. During the former, the algorithm calculates the energy required for a crack to initiate in a given sample. In the latter, the energy required to propagate a crack from initiation to final fracture is evaluated. The final outcomes of these two stages are the initiation strain energy release rate G_{init} and the propagation strain energy release rate G_{prop}, which are essentially these energies normalised. The distinction between the two values is visualised in the force-displacement curve shown in Figure 3.13.
Since the moment of crack initiation always corresponds to the moment in which the sample experiences the maximal load P_{max}, the energy expended to initiate the crack can be calculated as the area under the force-displacement curve from the start of the test to the point when the maximal load is experienced. The algorithm estimates that area using

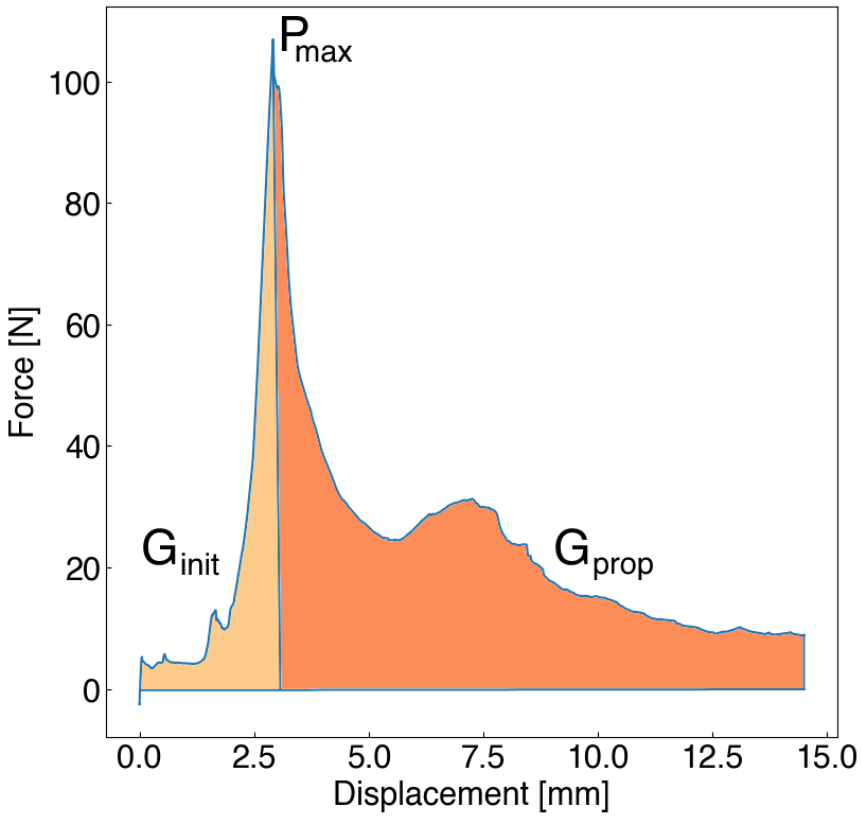

Figure 3.13: Initiation and propagation visualised. G_{init} represents the energy expended from the start of the test to the moment the crack initiates, hence the moment of maximal load before the load drop. G_{prop} represents the energy expended from that point until final fracture of the specimen.

the trapezoid rule, as shown in Equation 3.6.

$$U_Q = \sum_{i=2}^{N} \frac{u(i) - u(i-1)}{2} [F(i) + F(i-1)] \tag{3.6}$$

Where u and F are displacement and force, respectively, i is the index of the current data point and N is the index of the last data point, in this case the one corresponding to the maximal load. U_Q is the energy expended from the start of the test to crack initiation. However, it is not equal to the energy required to initiate a crack in the sample. Since LCP is not a perfectly rigid material, when the test begins the bolts indent themselves in the holes before starting to pull the sample apart, which also takes energy. In order to eliminate the influence of this effect on the data, a calibration CT specimen is also tested. It is identical in all ways to the sample shown in Figure 3.11 except that it has no notch. Therefore, all energy expended while loading it is only due to bolt indentation. By calculating the energy expended in the calibration sample up to the same displacement as experienced by the real sample in the moment of crack initiation, and then subtracting the energy of the calibration sample from that of the real one, one eliminates the contribution of bolt indentation, and is left only with the energy required to initiate a crack, U_{init}.

Of course, U_{init} is not very useful for comparing between this research and others, as it is affected by the sample's dimensions. For meaningful comparison, one must use the dimension-independent variable G_{init}, or the initiation strain energy release rate. Equation 3.7 reveals the necessary transformation to go from energy to energy release rate.

$$G_{init} = \frac{U_{init}}{bW\mu} \tag{3.7}$$

The denominator in this equation represents the geometry of the sample. b is its width, W is the distance from the centre of the loading hole to the back of the sample and μ is a special constant that accounts for the length of the initial crack a_{init}. For the CT sample, this length is equal to the distance along x from the centre of the loading hole to the tip of the notch (the crack tip). Equation 3.8 presents the exact formula used to calculate μ, obtained directly from the testing standard ASTM D5045. s is equal to the crack length a_{init} divided by W.

$$\mu = \frac{\left(1.9118+19.118s-2.5122s^2-23.226s^3+20.54s^4\right)(1-s)}{\left(19.118-5.0244s-69.678s^2+82.16s^3\right)(1-s)+2\left(1.19118+19.118s-2.5122s^2-23.226s^3+20.54s^4\right)} \tag{3.8}$$

Before the propagation analysis can commence, a correction in the data is necessary. During testing, the test was set to end when the current load has fallen to 1% of the maximal load, so that all the phenomena occurring after crack initiation could be properly studied. This value proved too conservative. Since the maximum loads in most cases either barely exceeded 100 N, or did not reach that value at all, the testing machine was essentially told to only stop the test once the load value drops to about 1 N. This value is so low that random noise often keeps the measurement value above this threshold. As a result, even after in reality the crack has completely propagated, the test continues, resulting in a long plateau region until the moment the user terminates the test manually. Since the propagation analysis takes into account all energy expended from crack initiation to the moment of final fracture, it becomes necessary to remove the plateau region, as it occurs after the part has fully failed. Hence, new end-of-test criteria are enforced in the Python code. The code checks when the slope of the force-displacement curve (calculated with the centred difference approach from Equation 3.5) reaches 0.02 or less, which corresponds to a flat or very slowly decreasing curve. Then, if the current load is 10% or less of the maximum, the force-displacement curve is truncated. The first criteria on its own is sufficient to correctly truncate samples with a smooth post-fracture curve, such as the one shown in Figure 3.14a. However, some samples may exhibit a hump, like the one in Figure 3.14b. In those samples, if only the slope criterion would be used, the code would trim the curve to before the hump, which is wrong as the sample has not failed completely yet.

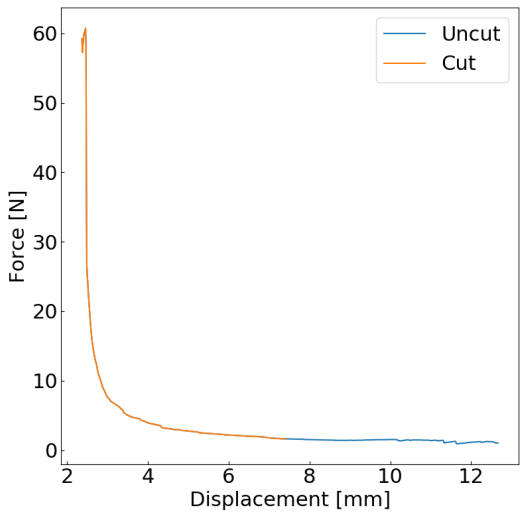

(a) Truncation in a sample with a smooth post-fracture curve. The "tail" of the curve is caused by noise preventing the test from finishing, even when the sample has fully failed, and is therefore cut off.

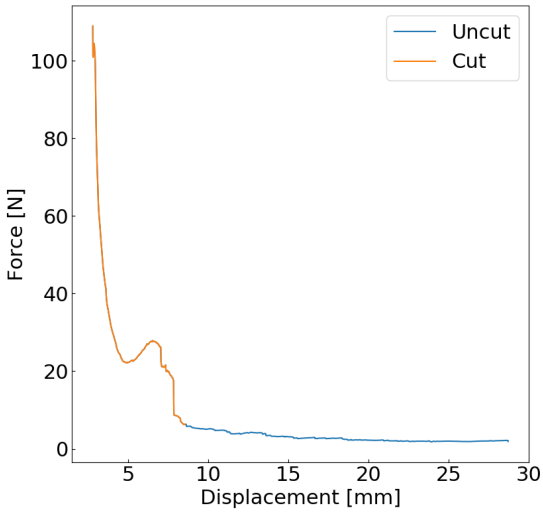

(b) Truncation in a sample with a hump in the post-fracture curve. The "hump" is useful data, so the code is modified to only cut after it.

Figure 3.14: New end-of-test criteria visualised

Using the corrected data, the code calculates the energy expended during crack propagation U_{prop}, using the trapezoid rule again. No correction for the penetration of the loading bolts is needed, since it is already accounted for in the initiation stage.

The standard ASTM D504 unfortunately only provides a way to calculate the initiation strain energy release rate (SERR). However, in their work Zhang et al [37] perform a similar experiment and do calculate the propagation SERR. The formula they use is given in Equation 3.9. It is the formula used in this code as well.

$$G_{prop} = \frac{\eta U_{prop}}{b(W-a_{init})} \quad ; \quad \eta = 2+0.522\frac{W-a_{init}}{W} \tag{3.9}$$

Where b is once again the sample width, W - the distance from the center of the loading hole to the back of the sample and a_{init} is the distance along x between the notch (crack) tip and the loading hole centre. η is a constant accounting for the initial crack size, similar to the constant ϕ which is used for initiation. After this step is completed, G_{prop} can be obtained for the tested sample, which allows comparison between samples using the different toughening approaches. It also allows G_{init} to be compared to G_{prop}.

4

Results

Introduction

This chapter presents the results for the experiments performed on the LCP samples. It is divided in two sections: one covering the outcomes of the fracture tests, and one for the tensile tests. Detailed reasoning, such as connecting these outcomes to physical phenomena suspected to be occurring, is the focus of Chapter 5.

4.1. Fracture tests

As mentioned in Chapter 3, the raw force-displacement data obtained from fracture tests of CT samples is used to evaluate the strain energy release rates for crack initiation and propagation, G_{init} and G_{prop}. In this section, these quantities will be presented in boxplots, with each boxplot representing one sample "family" - a group of samples using the same toughening approach and sharing the same parameter value. These boxplots allow comparison between the toughened and control (*UD*) samples, as well as the establishment of a relationship between fracture toughness and each of the three studied parameters.

4.1.1. Comparison with PLA

Before the effectiveness of the toughening approaches on LCP can be gauged, it is useful to put its toughness in perspective with that of the currently prevalent FFF printing material, PLA. The toughness plots for the two are presented in Figure 4.1.

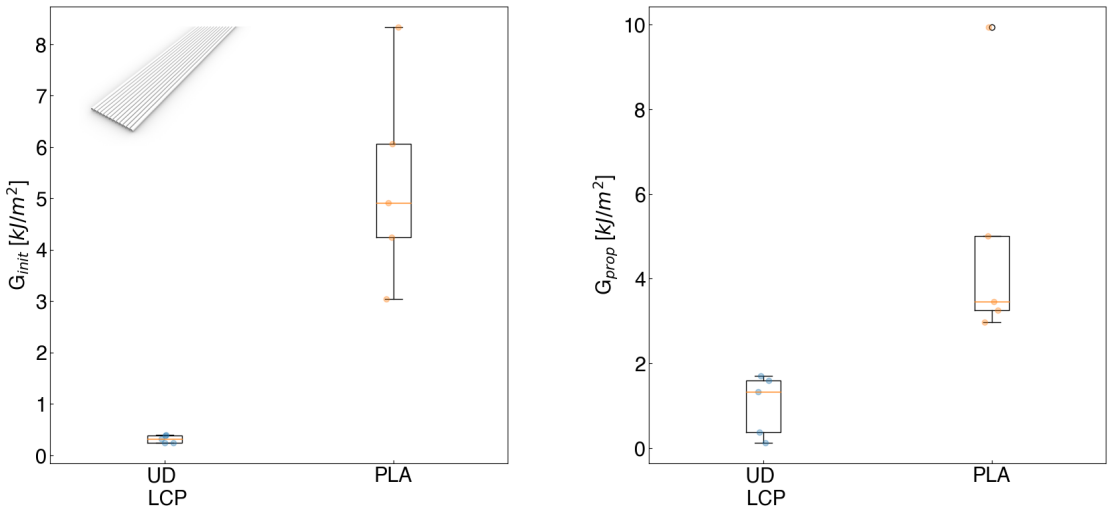

(a) Initiation

(b) Propagation

Figure 4.1: Mode I fracture toughness of the liquid crystal polymer (*UD LCP*) and polylactic acid (*PLA*) samples. PLA has a much higher toughness owing to its superior layer adhesion.

Due to its bad layer adhesion properties, LCP unsurprisingly has a very small G_{init} when compared to PLA. The gulf between the two materials is not as big for the propagation toughness, but in any case, it can be seen that LCP requires toughening in Mode I.

4.1.2. Matchstick approach

Of the three toughening approaches, the matchstick approach was the one hypothesised to be the least effective, as it is novel and still unproven. However, the data in Figure 4.2 reveals that a high overlap length corresponds to a better strain energy release rate than the control case, for both initiation and propagation. It is interesting that there is no significant difference in performance between the *OL*10 mm and *OL*20 mm samples. For the samples with only 5 mm of overlap, a worse toughness than the *UD* specimens is recorded.

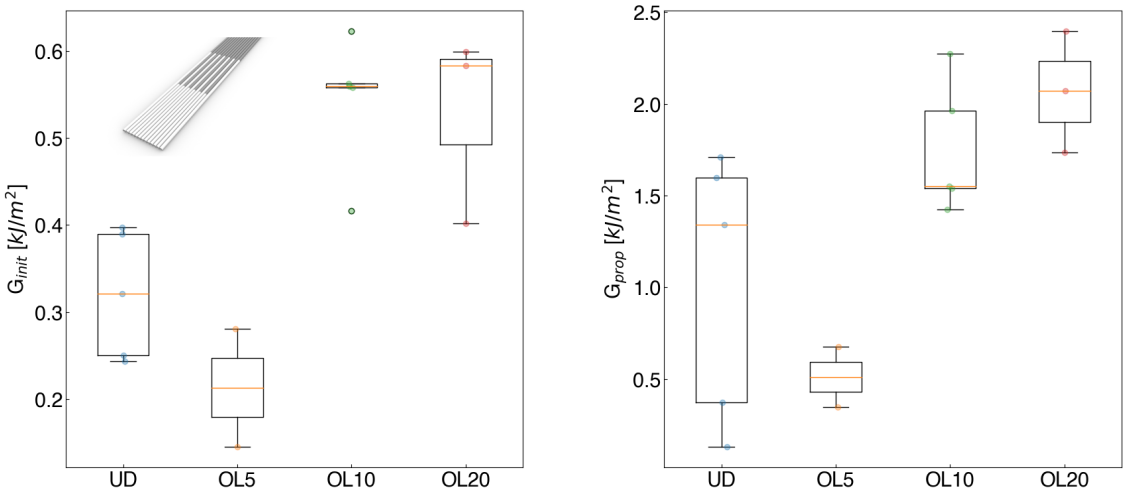

(a) Initiation

(b) Propagation

Figure 4.2: Fracture toughness of the matchstick (*OL*) samples compared to the control (*UD*) samples. Samples with a small overlap length perform poorly compared to UD. *OL*10 and *OL*20 perform well, and surprisingly similar to each other

It should be noted that *OL* samples with invisible microcracks are not represented in these plots. This type of defect causes a crack to develop at a different location than the desired one during testing, rendering the result invalid. Due to this, only two *OL5* mm samples and three *OL20* mm samples are studied, compared to five for all other specimen families.

4.1.3. Z-pinning

Based on the improvement in performance reported for composites in literature, z-pinning was hypothesised to be an effective toughening approach in LCP as well. Nonetheless, the toughness plots in Figure 4.3 reveal that not to be the case. For G_{init}, the fracture data exhibits a high level of spread. Some samples perform better than the control case, and some perform worse, but in any case the initiation toughness does not seem to be influenced by the z-pin density in a significant way. In the case of G_{prop}, the spread in the data is comparable to the one for the *UD* samples, but there is such overlap between the data ranges that a clear relationship between pin density and toughness cannot be established.

4.1.4. Sawtooth layers

The sawtooth layers were expected to be an excellent toughening approach due to the similarity with layer waviness, which has a proven toughening effect. The data in Figure 4.4 confirms this hypothesis. There seems to be a positive linear relationship between G_{init} and the sharpness angle ϕ, the main parameter of the sawtooth pattern. In the case of G_{prop}, the relationship is less clear. The 10° and 15° degree samples perform in the same range as the UD samples, with only a slight improvement as sharpness increases. On the other hand, the 20° specimens exhibit a significantly higher propagation toughness, on a similar level to PLA specimens.

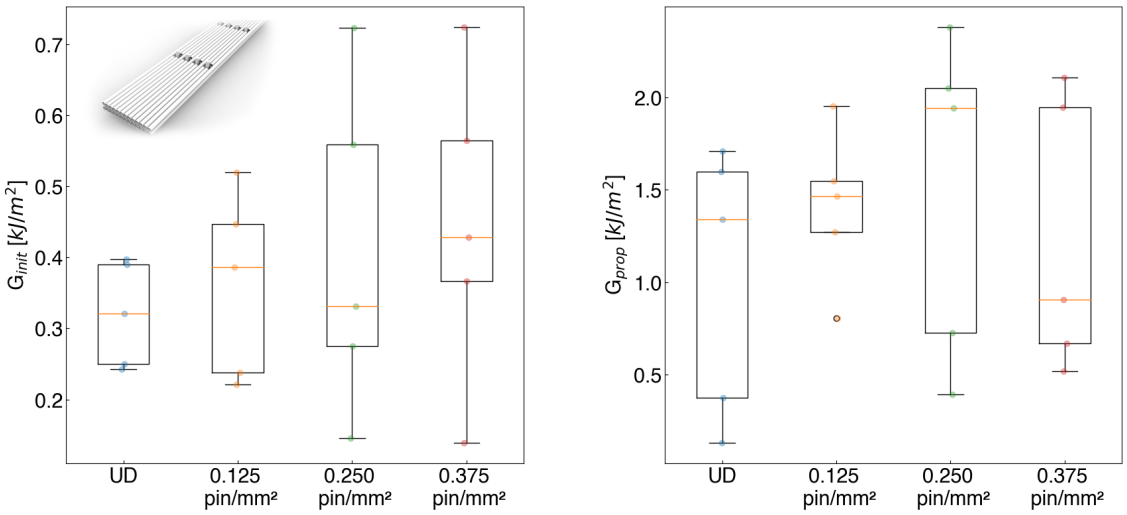

(a) Initiation

(b) Propagation

Figure 4.3: Fracture toughness of the z-pinned (*ZP*) samples compared to the control (*UD*) samples. The z-pin sample data exhibits a high spread and no clear trend.

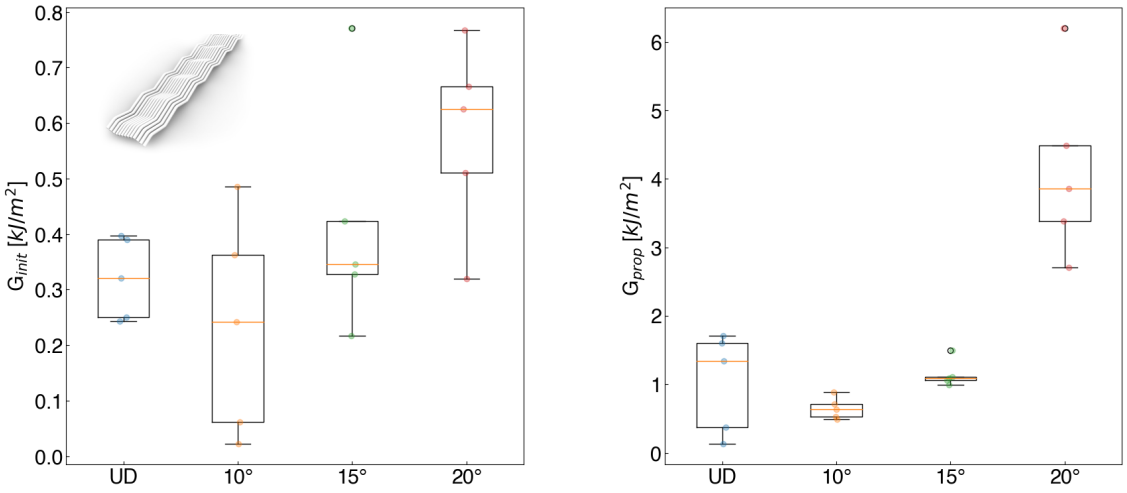

(a) Initiation

(b) Propagation

Figure 4.4: Fracture toughness of the sawtooth (*ST*) samples compared to the control (*UD*) samples. While the improvement in G_{init} is linear, G_{prop} scales faster, reaching values similar to PLA.

4.2. Tensile tests

In this section, the stress-strain curves obtained after the processing of tensile test data are displayed, once again grouped in such a way as to allow comparison between the control samples and those with toughening approaches. At the end of the section, the values for the elastic modulus, yield stress and ultimate stress are summarised for all specimen families in Figure 4.7. This is due to these properties not always being easy to read directly from the stress-strain curves.

4.2.1. LCP at different temperatures

All fracture specimens were manufactured using a nozzle temperature of 330 °*C* to minimise the microcracking in bulky samples mentioned in Chapter 3. The tensile specimens, being thin and slender, did not exhibit this issue. Due to this, while some of them were printed at the same temperature as the fracture specimens, other were printed at

the temperature of 300 °*C*. This was done to verify that LCP's alignment and tensile properties are affected by printing temperature, a finding reported in previous research [1]. Two sets of *UD* control samples were printed, one for each temperature. These two control sets are compared in Figure 4.5a.

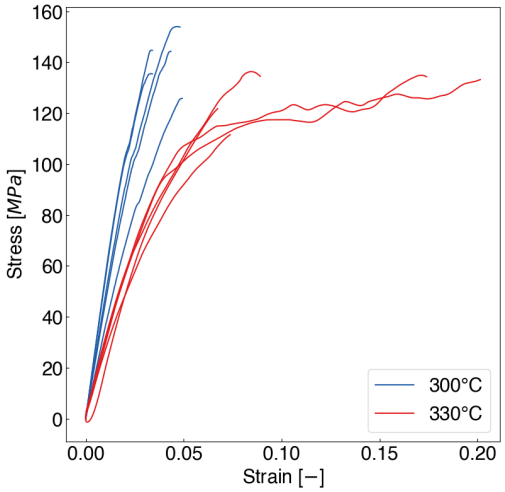

(a) Stress-strain curves for the control samples printed at different nozzle temperatures. A higher nozzle temperature results in a reduction of elastic modulus and ultimate stress.

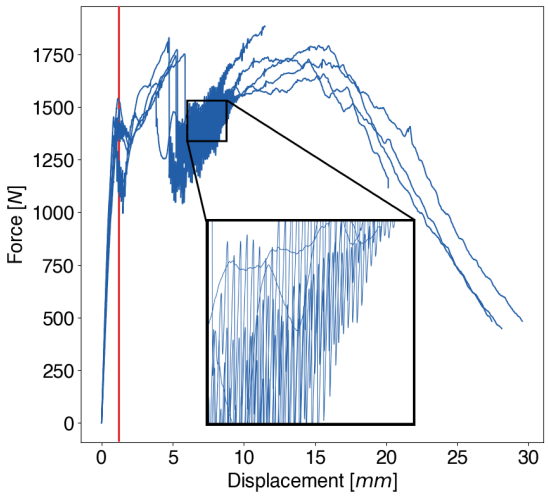

(b) 300 °*C* control sample curves before truncation. Note the severe slip oscillation past the line of truncation.

Figure 4.5: Results for the tensile tests of the control samples

As it can be seen, increasing the nozzle temperature reduces the yield and ultimate stresses of the samples, as well as the elastic modulus (the slope of the first section of the stress-strain curves). Nevertheless, Figure 4.5a may leave the false impression that the 330 °*C* specimens have a higher failure strain. That is untrue because the 300 °*C* curves have been severely truncated. This is necessary due to the machine grips slipping after the yield point during the tests of those samples, causing a characteristic oscillation in the curves post-yield, shown in Figure 4.5b. Slipping invalidates all data post-onset, hence the truncation, which is performed according to the criteria outlined in Chapter 3.

4.2.2. Matchstick approach

The matchstick approach specimens were printed at 300 °*C*, so in order to draw conclusions only about the effect of the matchstick approach, comparison is made with the control samples printed at the same temperature.The results of this are shown in Figure 4.6a. It can be glimpsed that the elastic modulus, yield stress and tensile stress are reduced in the *OL* samples compared to the *UD* ones. However, there is not much difference between the samples with different overlap length values.

4.2.3. Z-pinning

The z-pinned samples were printed at 330 °*C*, and are compared to the appropriate control specimens in Figure 4.6b. Like the matchstick approach specimens, the z-pinned ones exhibit a significant reduction in yield and ultimate stress when compared to the control samples. However, unlike the *OL* samples, the *ZP* ones have an elastic modulus similar in magnitude to that of the *UD* specimens printed at the same temperature.

4.2.4. Sawtooth layers

The sawtooth layers specimens were manufactured at 330 °*C*, and are presented alongside the corresponding control specimens in Figure 4.6c. The figure shows a negative relationship between the sharpness angle ϕ and the tensile properties of the samples. However, the sawtooth pattern also seems to cause an effect similar to strain-hardening after the yield point, with this "hardening" lasting longer the higher the sharpness.

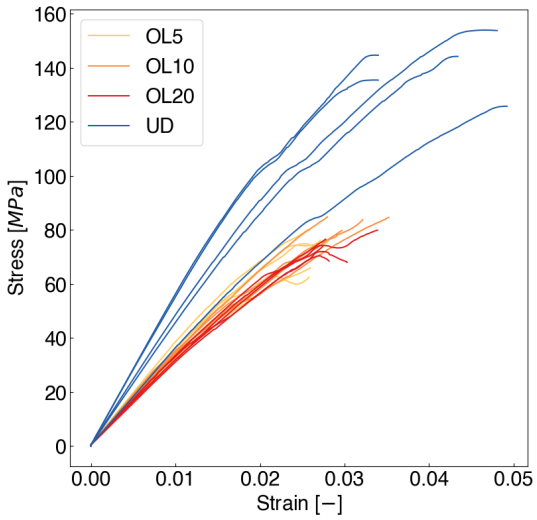

(a) Stress-strain curves for the matchstick approach samples. While introducing the matchstick approach reduces ultimate stress and elastic modulus, the actual overlap length seems to have no big effect.

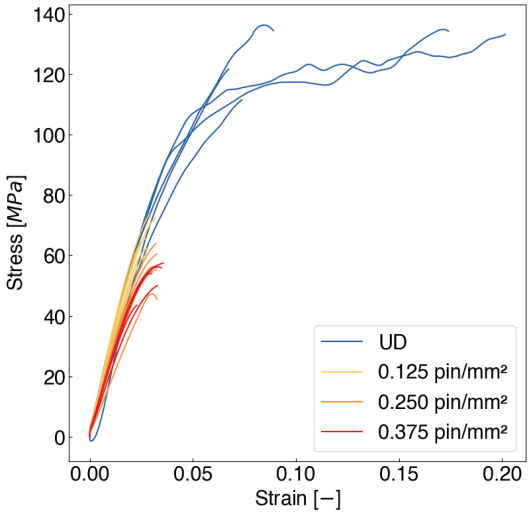

(b) Stress-strain curves for the z-pinned samples. Similarly to the matchstick samples, the presence of z-pins is more important than the value of the parameter, in this case the density.

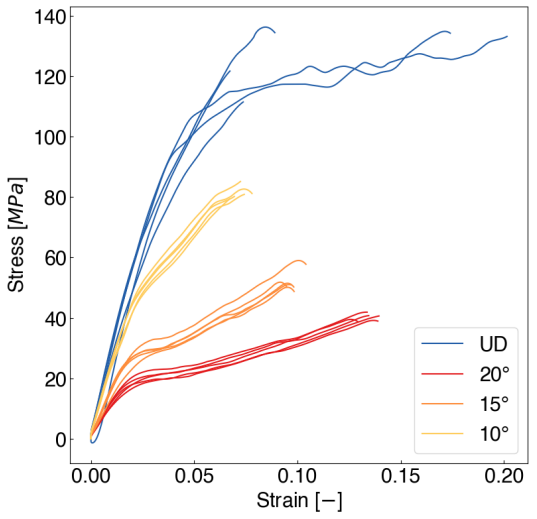

(c) Stress-strain curves for the sawtooth layers samples. Increasing the wave sharpness angle causes a matching reduction in elastic modulus and ultimate stress. It also seems to increase ultimate strain.

Figure 4.6: Results for the tensile tests of the toughened samples

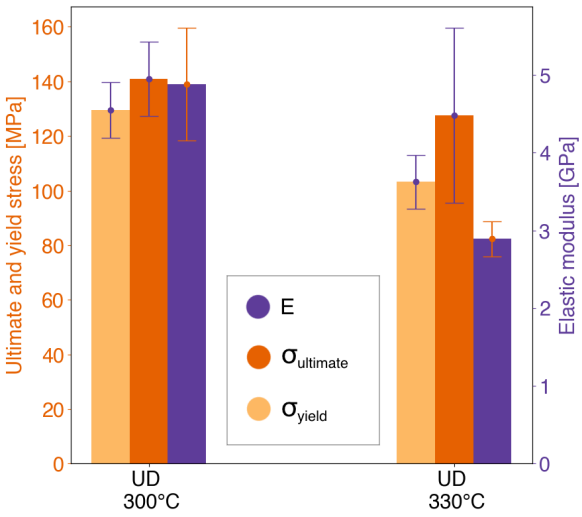

(a) Tensile properties of the *UD* specimens printed at different temperatures, summarised. The samples printed at a lower temperature perform better across the board.

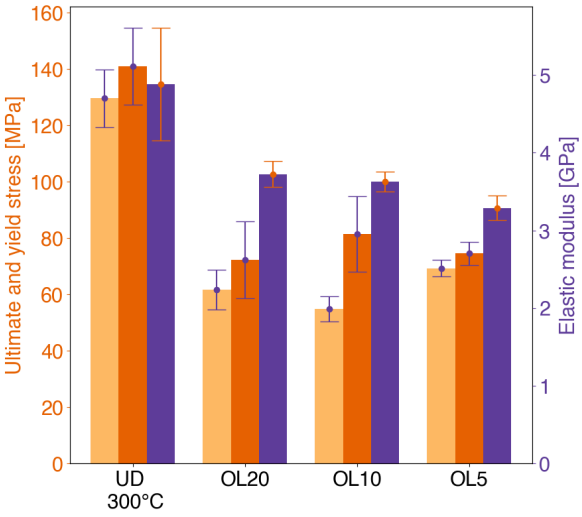

(b) Tensile properties of the *OL* specimens, summarised. While the matchstick specimens all perform worse than the *UD* ones, they do not differ a lot from each other.

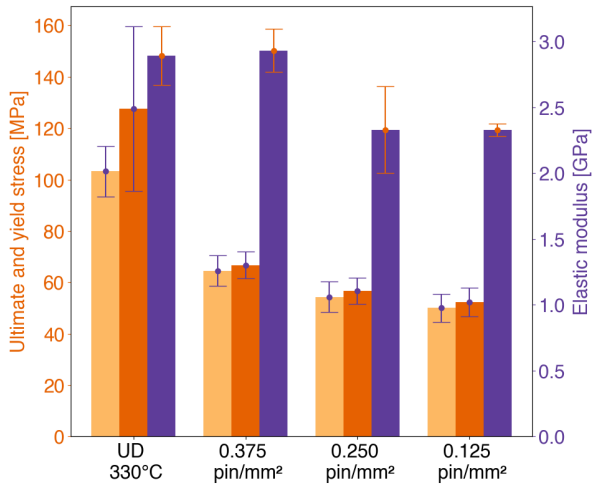

(c) Tensile properties of the *ZP* specimens, summarised. A similar behaviour to the *OL* specimens, with the exception of a higher elastic modulus.

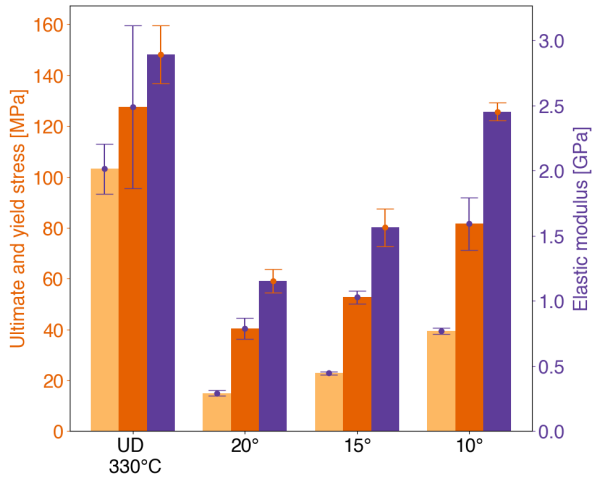

(d) Tensile properties of the *ST* specimens, summarised. Noticeable degradation as a function of the sharpness angle.

Figure 4.7: Summarised results of all tensile tests

5

Discussion

Introduction

In this chapter, the results presented in Chapter 4 are analysed, with the aim of understanding the effect each toughening approach has on LCP's Mode I fracture toughness, as well as the physical phenomena underlying that effect. The chapter is divided in three sections. In the first, the influence of fiber bridging on the propagation toughness G_{prop} is assessed, and efforts are made to separate it from the influence of the toughening approaches. In the second, the impact of each of the three approaches on the initation and propagation toughness is quantified, and hypotheses are made as to what is the physical principle behind it. The effects on the tensile properties of LCP are also discussed. The last section deals with the shortcomings of the chosen method for measuring the effect of fiber bridging.

5.1. Fiber bridging in liquid crystalline polymers

While Figures 4.2b-4.4b already allow some conclusions to be drawn about the effects on G_{prop} of the matchstick overlap length, z-pin density and layer sharpness angle, those conclusions would not be fully accurate. There is a hidden variable at play in the LCP samples, influencing the results alongside the toughening approaches. That variable is fiber bridging. As mentioned in Chapter 2, fiber bridging creates a cohesive zone behind the crack tip, causing energy to be dissipated by the loading of the fibers. The microscope images of the fracture surfaces for different samples (shown in Figure 5.1) reveal that the extent of the bridging (i.e. the size of the process zone) is not constant for all samples. Hence, a fair comparison between them cannot be drawn before fiber bridging is accounted for.

One way to quantify the extent of the bridging is by looking at the marks it leaves on the fracture surfaces of the samples, visible in Figure 5.1. The PLA samples exhibit no bridging and thus have (relatively) smooth fracture surfaces. The UD,OL and ZP samples experience fiber bridging, and as a result their fracture surfaces are very chaotic. The ST samples also have bridging. In the $ST20°$ samples specifically, this is to a much greater extent than other LCP samples. To quantify the extent to which this toughening phenomenon affects the results, the surface-averaged roughness S_a is measured for the fracture surfaces of each sample tested. This parameter is chosen because of the visible correlation between fiber bridging and fracture surface smoothness/roughness.

The discussion about the influence of the three toughening approaches on LCP's propagation fracture toughness will be based not only on G_{prop}, but also on the ratio G_{prop}/S_a, or "roughness-corrected toughness". The idea behind this second parameter is to distinguish between the samples that are tough only because of fiber bridging (which would have a high S_a, hence a small roughness-corrected toughness), and the samples that are tough only thanks to the toughening approach employed (which would have a low S_a, hence a high roughness-corrected toughness).

5.2. Toughening approach influence on the material properties of liquid crystalline polymers

5.2.1. Matchstick approach

In Chapter 4, it was determined that the matchstick approach lowers LCP toughness at a low overlap length (5 mm) and increases it at a high one. However, $OL10$ mm and $OL20$ mm showed values for G_{init} and G_{prop} so similar that it was unclear if increasing OL beyond 10 mm is beneficial. The roughness analysis shown in Figure 5.2 answers this

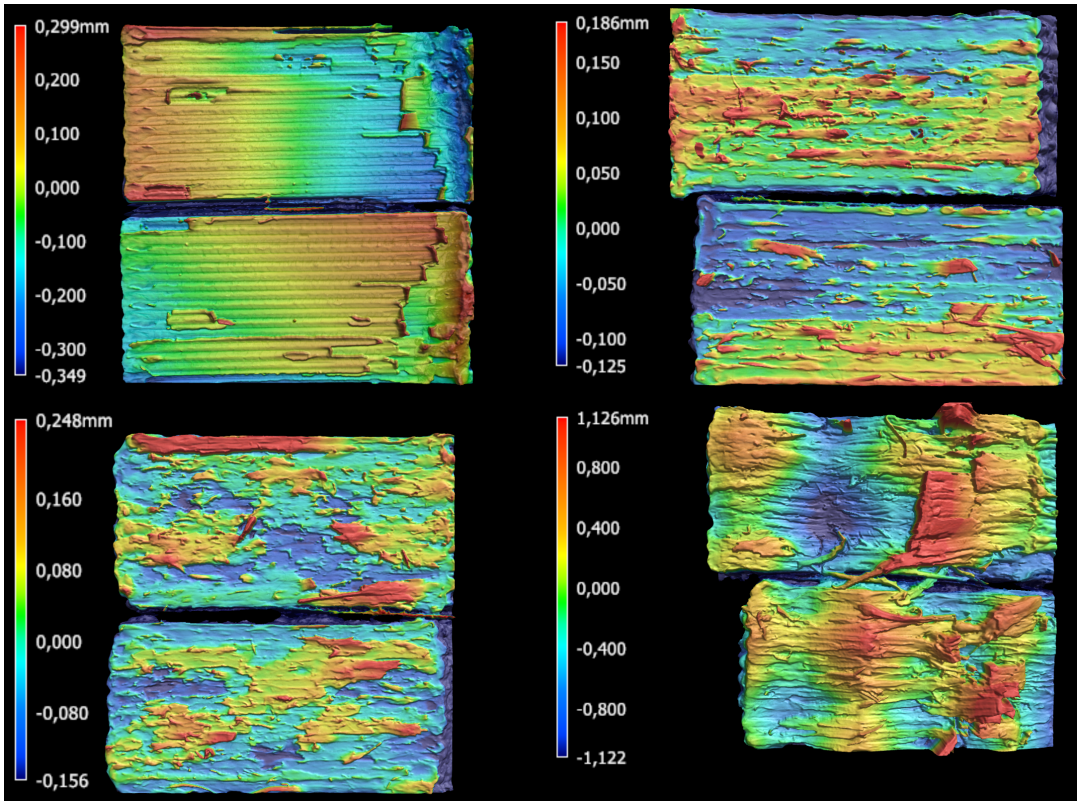

Figure 5.1: Fracture surfaces of different samples. From the top-left, clockwise: polylactic acid (PLA) specimens, unmodified LCP specimens (UD), specimens with 20° sawtooth waviness (ST20°) and specimens with 20 mm matchstick overlap (OL20 mm). Some samples exhibit significantly more surface roughness than others, with a fourfold difference between PLA and ST20°

question. There is a positive relationship between matchstick overlap length and propagation fracture toughness, and while $OL10$ mm samples have a similar G_{prop} to $OL20$ mm ones, this is only due to them experiencing more fiber bridging (hence their lower G_{prop}/S_a).

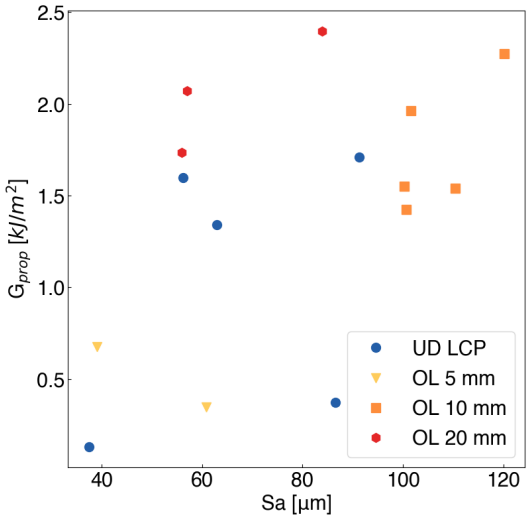

(a) Propagation toughness versus surface roughness

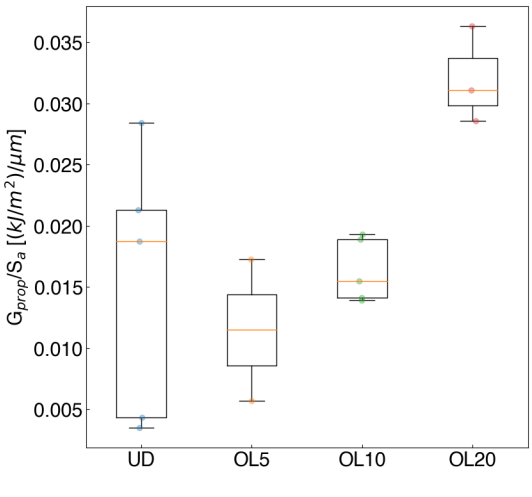

(b) Roughness-corrected toughness plots

Figure 5.2: The influence of the fracture surface roughness S_a on the propagation fracture toughness of the matchstick (OL) samples. $OL10$ specimens exhibit more bridging on average than all other samples. Unlike $OL20$ samples, their toughness is more due to this than the toughening approach itself. This discrepancy is reflected in the G_{prop}/S_a values of both groups.

A possible reason behind the toughening effect of the matchstick approach could be that by using lines shorter than the full length of the sample, LCP is becoming more similar to wood, and is therefore benefiting from the same toughening mechanisms. Vašic et al [24] report that fibre bridging in wood is caused by wood grains being peeled off behind the crack tip as the crack faces separate, and then get loaded as a beam before finally tearing. A longer wood grain (or in this case, matchstick) takes longer to peel and to tear, meaning it is better at toughening. Nairn et al [26] add that a greater grain length is also more conducive to fiber bridging. The same effect can be seen here, with the *OL*5 mm samples having a very low surface roughness (hence little bridging) in comparison to the samples with a higher overlap length.

Whereas the introduction of the matchstick approach has a beneficial effect on the fracture toughness of LCP, the opposite is true for the material's tensile properties. As shown in Figure 4.6a, a loss of 33% in elastic modulus and 47% in yield and ultimate stress results from changing from *UD* samples to *OL*20 mm ones. The smaller overlap matchstick samples perform only slightly better. The cause of this reduction is due to load path interruption. When the *UD* samples are loaded in tension, these paths comprise only continuous lines, which are strong. In the *OL* samples, the load instead passes through separate matchsticks, and load transfer via the matchstick overlap regions must occur. Since LCP has great mechanical properties along the printed line due to its anisotropy, but subpar adhesion properties, a reduction in tensile properties occurs. A similar logic applies when comparing additively manufactured continuous CFRP and long fibre CFRP. In the first case, the strong fibres carry most of the load, while in the second, load transfer between fibres passing through the weak matrix results in earlier failure [38].

5.2.2. Z-pinning

Figure 4.3 shows that the z-pins do not noticeably improve or reduce the initiation and propagation toughness in LCP. Their presence only increases the variance in the data. Knowing that the extent of fiber bridging in LCP can vary, as evidenced by the matchstick samples, one would assume that this large spread is caused by bridging, at least for propagation. Figure 5.3 verifies that assumption to an extent. The z-pinned samples are shown to exhibit a wide range of fracture surface roughness, without any pattern.

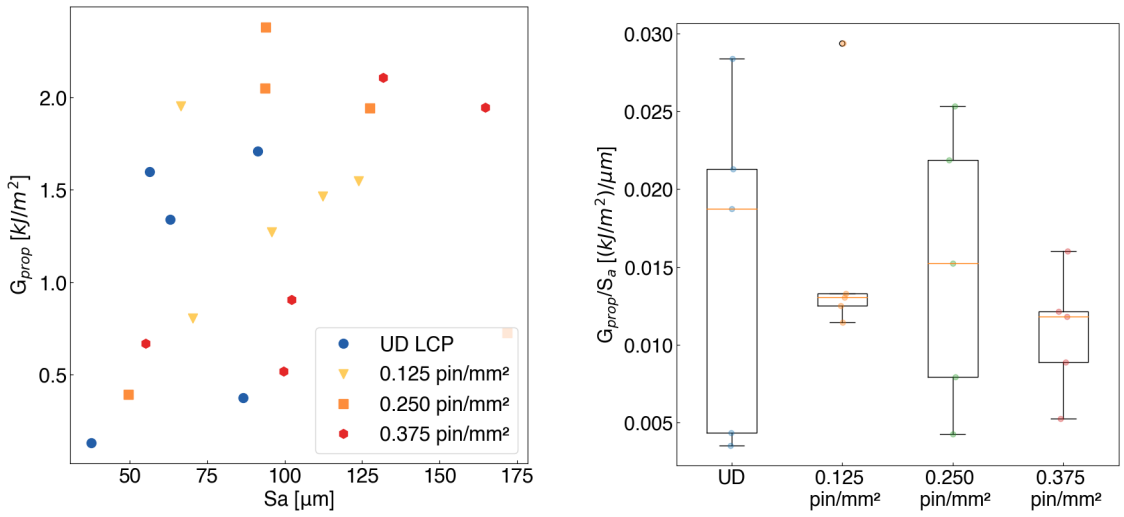

(a) Propagation toughness versus surface roughness

(b) Roughness-corrected toughness plots

Figure 5.3: The inconclusive influence of the fracture surface roughness S_a on the propagation fracture toughness of the z-pinned (ZP) samples. All z-pin densities exhibit a similar spread of surface roughness. With S_a accounted for, all specimens perform similarly to the control ones.

However, even with fiber bridging accounted for, the data does not show any correlation between the z-pin density and the propagation fracture toughness. Furthermore, the plot for the roughness-corrected toughness demonstrates that all but one z-pinned samples perform within the margins of the control specimens. The conclusion is that the current implementation of z-pinning is wholly ineffective as a toughening approach for additively manufactured LCP. A possible reason for this can be seen in Figure 3.8. The z-pins, which are supposed to form a monolithic rod going through all the layers, instead appear as a loose stack of drop-like shapes. This weaker geometric shape is likely why the z-pins fail to reinforce the samples.

As for the tensile properties, the z-pinned samples perform better than the matchstick approach ones. The reduction in yield and ultimate stress is once again about 50%, but the elastic modulus only reduces 20% for the specimens with 0.250 and 0.375 pin/mm^2. The 0.125 pin/mm^2 samples exhibit no significant drop in the modulus. This higher stiffness can be explained by the fact that the z-pinned samples comprise of both matchsticks (in the lines that have pins) and continuous lines (in the other lines). The longer lines serve to reinforce the sample.

5.2.3. Sawtooth pattern

Figure 4.4 reveals that the $ST20°$ sample family improves the average initiation fracture toughness of LCP by a factor of two. For propagation, the increase is fourfold. While the $OL20$ mm family (second best in toughening) almost matches the G_{init} improvement, the propagation toughness increase it provides is less than 1.5 times. As the sawtooth layers are the most promising of the toughening approaches studied, most attention is dedicated to them.

The gradual improvement of the initiation toughness as the sharpness angle ϕ is increased can be explained through the mode mixity phenomenon described in Chapter 2. While globally the sample is loaded in Mode I, on a local level, the crack initiation site experiences a mix of Mode I and Mode II loading due to the angled layers. The higher the sharpness angle, the more Mode II is present in this mixture. Since materials have a higher fracture toughness in the shear opening mode than the tensile one, the Mixed Mode I/II toughness (which is the relevant one at the crack tip) grows larger and larger as the angle increases.

Mode mixity resumes being a factor during crack propagation. To assess its influence, the effect of fiber bridging must be accounted for through a roughness analysis. This is shown in Figure 5.4. Note the switch of the roughness parameter from S_a to S_{a_corr}, as previously discussed in Chapter 3. The boxplots for the roughness-corrected toughness reveal that even with the bridging taken into account, there is still improvement in toughness as ϕ increases, proving that mode mixity is at play.

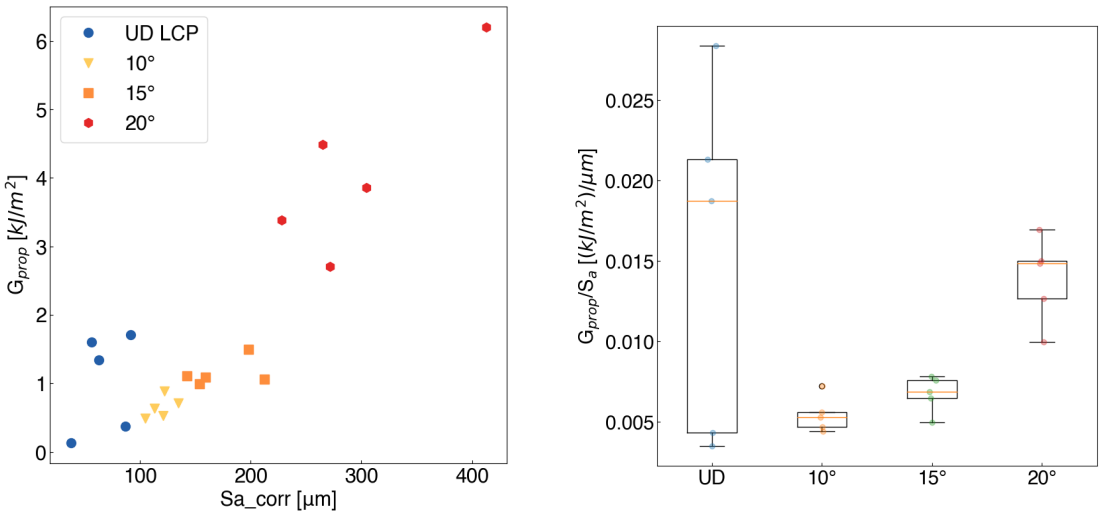

(a) Propagation toughness versus surface roughness

(b) Roughness-corrected toughness plots

Figure 5.4: The influence of the fracture surface roughness S_a on the propagation fracture toughness of the sawtooth (ST) samples. S_a is correlated to the layer sharpness angle ϕ. However, even once surface roughness is accounted for, toughness still increases at higher angles, displaying the beneficial effect of fracture mode I/II mixity at the crack tip.

Nevertheless, the influence of mode mixity on propagation is not as simple as it initially appears. The extent of fiber bridging (represented by the fracture surface roughness) increases with the layer sharpness angle, whereas it is uncorrelated to the matchstick overlap length and z-pin density. One possible explanation for this relationship is that the presence of Mixed Mode I/II loading at the crack tip is more conducive to lines shearing off and bridging the crack than pure tension is. However, one would then expect a mere linear improvement in G_{prop} as the surface roughness increases, whereas the relationship in Figure 5.4 is more quadratic in character. Therefore, the mode mixity must not only be causing more fibers to be created in the process zone, but it must be allowing these fibres to carry more load, increasing their crack shielding effect. Digital image correlation pictures taken during testing and shown

in Figure 5.5 lend credence to this hypothesis. Not only can more fibres be seen bridging the crack at higher layer sharpness angles, but those fibres are loaded more, causing high strain to be distributed along the top and bottom crack surfaces instead of being concentrated at the crack tip. Sawtooth layers and fiber bridging exhibit incredible synergy, with a combined toughening bigger than the sum of their separate effects.

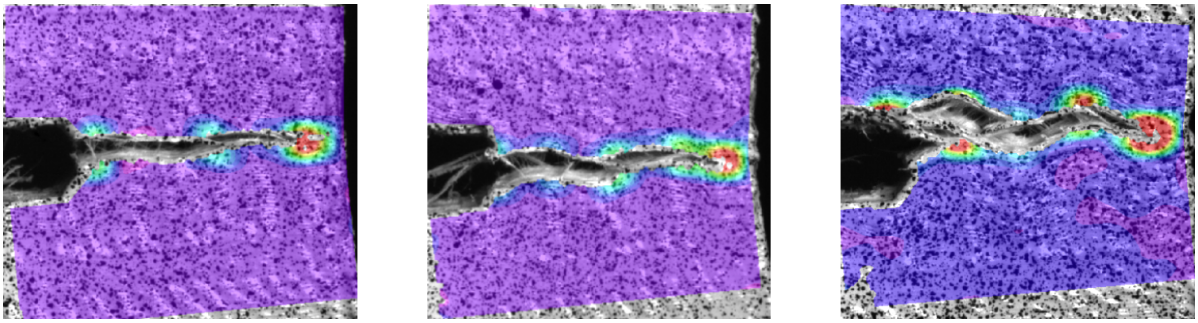

Figure 5.5: Digital image correlation (DIC) images of the sawtooth layer samples. From left to right: 10°, 15° and 20° sawtooth waviness. Specimens with a higher waviness not only have more fibers bridging the crack, but those fibers also carry more of the load, alleviating the load at the crack tip.

Unfortunately, the toughening from the sawtooth layers comes at the price of good tensile properties. The sample family that exhibits the highest toughness ($ST20°$) is also the worst in tension, with a reduction of 60% in elastic modulus, 85% in yield stress and 70% in ultimate stress compared to a UD specimen printed at the same temperature. This is due to LCP's nature as an anisotropic material. In the control specimens, the direction with the best mechanical properties (along the print line) is aligned with the testing direction because the layers are flat, ensuring the best possible performance. However, in sawtooth layer specimens, most of the material is at an angle of $\pm\phi$ to the loading direction, causing tensile properties to lower as the sharpness angle increases.

However, Figure 4.6c proves that the introduction of sawtooth layers triggers a behaviour similar to strain-hardening in the samples. Although all sawtooth samples yield at a smaller stress compared to the UD ones, this "strain-hardening" postpones final failure until a higher strain value. In contrast, matchstick and z-pinned samples fail in a brittle manner. Digital image correlation reveals the cause of this phenomenon to be the straightening out of the sawtooth layers, as seen in Figure 5.6. The peaks and valleys of the specimen experience the highest strains as the straightening takes place.

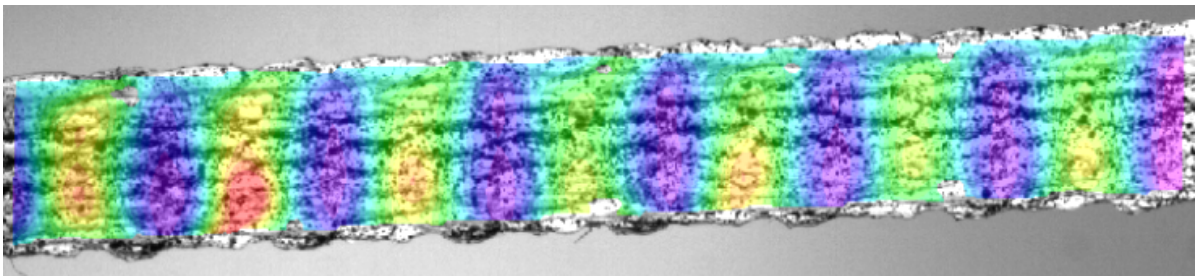

Figure 5.6: Digital image correlation (DIC) image of strain concentrations in the peaks and valleys of a sawtooth tensile specimen. This is caused by the layers being straightened during the test.

This phenomenon can be of interest if a high yield strain is desired above other tensile properties, since all five $ST20°$ specimens experience final fracture at a strain value of almost 0.15. For comparison, the z-pinned specimens printed at the same temperature fail at about 0.03 strain, and while two of the control specimens fail at a higher strain than the sawtooth samples, all others fail at a strain of about 0.05.

5.3. Limitations of the fiber bridging analysis

Quantifying fiber bridging through the analysis of the fracture surfaces proved to be a valuable tool in assessing the actual toughening each of the three approaches is providing to LCP. For the sawtooth layers, it is also instrumental in revealing the interactions between mode mixity and fiber bridging. However, more careful consideration reveals that the roughness-corrected toughness method is flawed, and does not fully represent the effect of fiber bridging.

Figure 5.7a shows the G_{prop} of the control specimens versus their fracture surface roughness. Since all samples fit within the same range of roughness, but three exhibit significantly higher toughness, one would assume there is some other toughening effect at play here. That is not the case. Test footage reveals that these three samples exhibit a degree of fiber bridging, while the other two do not, hence the difference. However, the fiber bridging in this case is highly local, with big fibers on only a few spots on the fracture surface. Since the parameter used for roughness S_a is taken as an average over the whole surface, that results in these fibers getting "smeared out" and the sample's roughness being brought down to the same level as that of the samples with no bridging. Due to this, roughness-corrected toughness does not account for all fiber bridging, only for that which is present over the entire fracture surface.

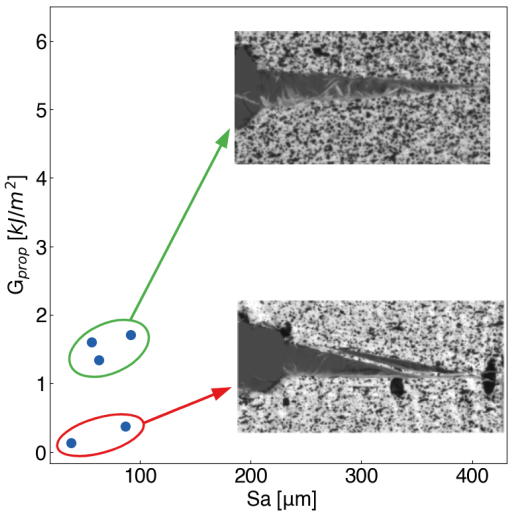

(a) Due to fibers not covering enough of the fracture surface, three control specimens exhibit an artificially low S_a, even though bridging impacts the toughness.

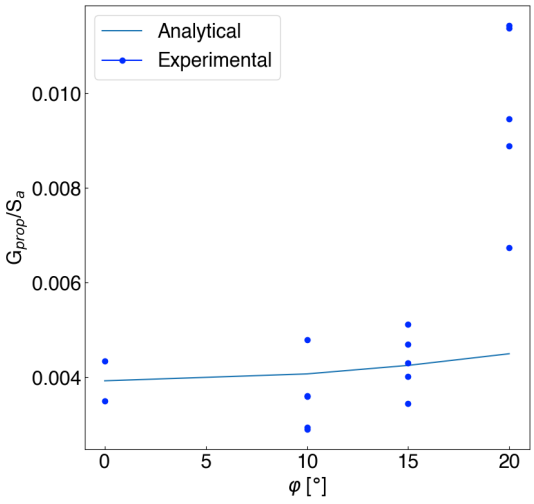

(b) Output of the analytical bent-crack equation compared to the roughness-corrected propagation toughness of tested ST samples. The fibers being more effective at bridging due to mode mixity is not modelled analytically, hence the mismatch.

Figure 5.7: Deficiencies of the roughness-corrected toughness parameter

Furthermore, while roughness-corrected toughness can account for the extent of fiber bridging (i.e. what part of the fracture surface is covered with fibres), it cannot account for how effective the fibres are in shielding the crack, which is something that differs per toughening approach. This can be seen from the validation of the test results for the sawtooth samples. The validation method employed is the bent-crack formula, an equation that evaluates the increase in strain energy release rate when the crack path changes from straight to a bent one, as is the case for wavy or sawtooth layers [34]. The formula is presented in Equation 5.1. Though originally using amplitude and wavelength of the layer as inputs, for ease the wave sharpness angle is used here. Since ϕ mathematically derives from A and λ, this is not an issue.

$$\frac{G_{bent}}{G_{flat}} = \frac{2}{1+[1+4\pi^2(A/\lambda)^2]^{-1/2}} = \frac{2}{1+[1+4\pi^2(tan\phi/4)^2]^{-1/2}} \tag{5.1}$$

This equation can evaluate the expected effect of toughening only due to the geometry of the sawtooth layers, or the effect of mode mixity without accounting for fiber bridging. This can then be compared to roughness-corrected toughness measured from the actual samples, which should also (theoretically) be free of influence from fiber bridging. This comparison is displayed in Figure 5.7b. As the reference value for the flat layers, the average G_{prop}/S_a of the two lowest toughness UD samples has been used. This is due to them experiencing almost no fiber bridging and hence being a good reference point. It can be seen from the figure that the roughness-corrected toughness of the $ST10°$ and $ST15°$ samples is well predicted by the bent-crack equation. Therefore, for low sharpness angles, the mode mixity effect accounts for most of the toughening. However, the $ST20°$ samples have a much higher roughness-corrected toughness than predicted. This is because of the synergistic effect mentioned previously. It can be concluded that the roughness analysis can account for more fibers being created during fracture, but not for those fibers exhibiting higher strains and hence shielding the crack more.

6

Conclusion

Introduction

In this chapter, all findings of this research are summarised, and conclusions about the effects of the studied toughening approaches are drawn. The chapter is divided in three sections. In the first, the significance of this project is established, with a view to LCP's position as a promising material in the aerospace industry. Next, each of the toughening approaches is judged, and their usefulness is discussed. In the last section, recommendations about further directions research could take are presented.

6.1. Significance of the current work

As mentioned in Chapter 2, Vectra A950 is a material with good tensile properties that compares favorably with composites commonly used in aerospace structures, even more so when fused filament fabrication is the manufacturing method of choice. The only drawback of the material is its low layer adhesion, which leads to a low fracture toughness. While annealing is one way to improve that, it renders the sample almost unrecyclable [1] as permanent cross-links form between layers. By employing toughening approaches inspired by nature on Vectra for the first time, the current project manages to achieve high interlaminar toughness without sacrificing recyclability. The beneficial effect of these approaches can be seen from Figure 6.1, which shows the *UD* control specimens with the best performing sample family for each toughening approach.

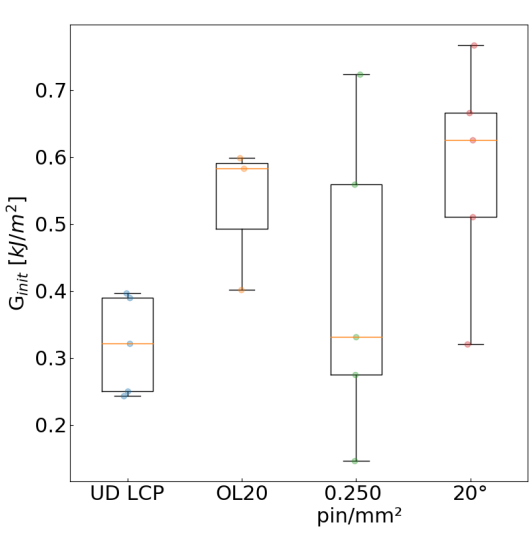

(a) Initiation toughness of the best families

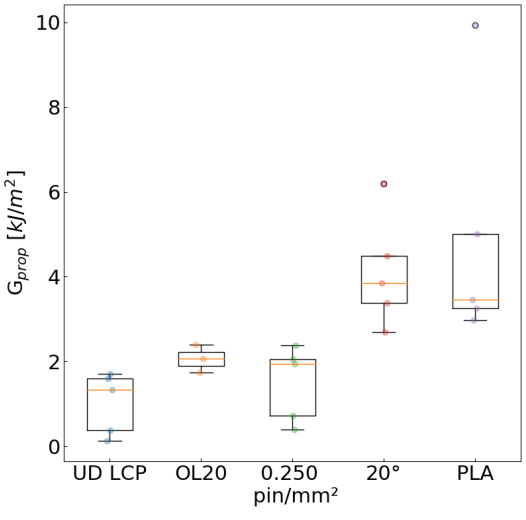

(b) Propagation toughness of the best families. PLA included for comparison with sawtooth specimens.

Figure 6.1: The influence of the toughening approaches on the fracture toughness of LCP. The matchstick approach and sawtooth layers are both effective at exploiting the shaping freedom of additive manufacturing to improve G_{init} and G_{prop}

The matchstick approach is another area in which this project makes strides. While this approach has been used before to introduce greater shaping freedom to additive manufacturing [39], it has never before been considered as a way to improve Mode I interlaminar toughness. This project studies the relationship between the matchstick overlap length and the fracture toughness in detail, and establishes a positive connection between the two, similar to the one present in wood.

This relationship is due to the important role fiber bridging plays during fracture in samples additively manufactured from Vectra A950. The current research studies this phenomenon in LCP for the first time and quantifies its importance in improving the propagation toughness of LCP specimens. Furthermore, new synergies are discovered between fiber bridging on one side and the matchstick approach and sawtooth layers on the other. These provide a toughness increase beyond the one expected from the sum of both effects. This is especially clear for the sawtooth layers, where the synergy allows LCP to reach a G_{prop} value comparable to that of PLA, as evident from Figure 6.1b.

Last but not least, this research is the first to study the fracture toughness of additively manufactured LCP at all, since the use of the material in this field only dates back to 2018 [1]. It can serve as a starting point for further research into the field of toughened LCP and fiber bridging in LCP.

6.2. Main conclusions

The first fact established by the research is that in the absence of any toughening approaches, Vectra A950 has a fracture toughness inferior to the commonly used PLA, with G_{init} being on average 94% lower and G_{prop} 79.1% lower. The better layer adhesion properties of the former material result in a higher fracture toughness that even fiber bridging cannot compensate for. To reduce this disparity, toughening approaches were applied to LCP. The following paragraphs present the results thereof.

6.2.1. Matchstick approach

Contrary to the initial expectation, implementing the matchstick approach has a positive influence on the fracture toughness (in both initiation and propagation). This influence scales with the selected control parameter- the matchstick overlap length OL. The samples with the highest overlap length (20 mm) exhibit an improvement of 65% on average for G_{init} and 100.5% for G_{prop} when compared to the values for untoughened LCP. This toughening may originate from the matchstick approach giving LCP a more wood-like structure. Since LCP as a hierarchical material is already similar to wood, the matchstick approach may be enough to trigger the same toughening mechanisms.

Unfortunately, the introduction of the matchstick approach worsens the tensile properties of LCP, with reductions of 32.6% for the elastic modulus and 47.1% for the ultimate stress when comparing matchstick samples with 20 mm overlap with the UD control specimens. This is due to forces now having to be transferred along the weak interface between print lines instead of only following the printed lines. The matchstick approach also causes an increase in manufacturing time of up to 39.5% for the 20 mm overlap samples.

6.2.2. Z-pinning

Though this research successfully reproduces the work of C.Duty et al [28] in applying z-pins as a reinforcing technique in additive manufacturing, in the end, this "toughening" approach provides little to no toughening. The z-pin density is correlated neither to initiation nor to propagation fracture toughness. Furthermore, the z-pin data has such a significant spread that it is meaningless to compare average toughness values with the control samples. Even though some samples exhibited better G_{prop} during testing, this was later proven to be due to fiber bridging, and not the z-pins themselves. The reason for this ineffectiveness can be glimpsed from microscope images of the cross-sections of the samples, shown in Figure 3.8 and also in Figure 6.2 for easier reference. The fact that the pins are shaped like drops instead of rods and do not connect very well to each other is very likely the reason they fail to provide toughening to the samples.

Z-pins are also not beneficial to the tensile properties of LCP, causing a 19.4% reduction in the elastic modulus and a 51.5% reduction in the ultimate stress. This is due to the same reason as the matchstick samples. Since printing z-pinned samples also significantly complicates the manufacturing process and requires up to twice as much time to print compared to control samples, there is no point in using the current version of z-pinning.

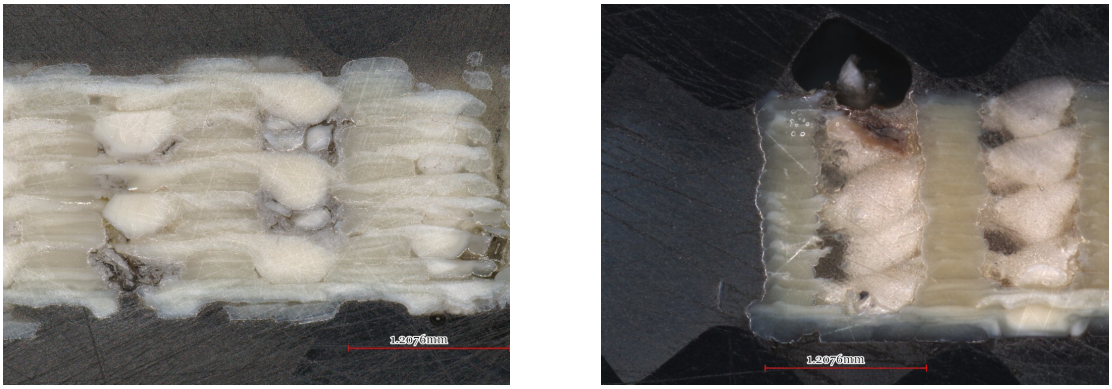

(a) 6-layer z-pins

(b) 4-layer z-pins

Figure 6.2: Z-pin deformations. It is theorised that the "stack of drops" shape assumed by the pins during printing is not effective as a reinforcement structure, hence the failure of z-pins to toughen the material.

6.2.3. Sawtooth layers

Inspired by the wavy layers employed by, among others, Mencattelli and Pinho [3], the sawtooth layers deliver on the initial expectations to improve interlaminar toughness. A positive correlation between the wave sharpness angle ϕ and both initiation and propagation fracture toughnesses has been established. The ST20° samples perform the best, showing an improvement over the control samples of 80.6% in G_{init} and 300.3% in G_{prop}. This makes sawtooth layers the most effective toughening approach of the three considered. The increase in propagation toughness is impressive. It allows LCP to achieve 83.7% of the G_{prop} for PLA, despite the latter having much better layer adhesion.

The relationship between G_{init} and ϕ is more or less linear and can be attributed to the Mixed Mode I/II fracture at the crack tip, with shear playing a more important role as the angle increases. However, in the G_{prop} case, the ST20° samples perform exponentially better than samples with a smaller angle. This is due to a synergy between the fibre bridging phenomenon and the mode mixity loading conditions, where the presence of Mode II both causes more fibers to develop in the process zone and allows these fibers to carry more load, postponing tearing. This synergy makes sawtooth layers a highly promising toughening approach well suited to LCP.

The toughening provided by the sawtooth layers comes at the cost of good tensile properties, with ST20° samples showing an elastic modulus 60 % lower than that of the control specimens, and an ultimate stress 70% lower. Increasing ϕ results in a loss of tensile properties, as the strongest material direction of the sample (along the printed LCP lines) moves progressively out of alignment with the loading direction. Printing sawtooth layers is also time-intensive, as ST20° samples take 2.23 times longer to print.

7

Recommendations for further research

Introduction

Although this project has made many interesting discoveries in the field of fracture toughness of additively manufactured Vectra A950, there are some places were the analysis had to be simplified or shortened due to the lack of time. A follow-up project would do well to focus on those areas to complete the picture. Furthermore, there are other interesting directions this research could have taken that remain completely unexplored. They will also be presented in this chapter.

7.1. Limitations of the current research

The first and most pressing issue that future research should tackle is the problem of inter-layer cracks appearing in bulky LCP parts. As shown by this project, increasing the printing temperature mitigates this issue, but does not solve it completely. If LCP is to used commercially in the aerospace industry, a failure rate of 10% is unacceptable (five out of fifty CT samples had cracks).
Due to these failures, which were all matchstick approach samples, the reliability of the conclusions drawn about this toughening approach in the current research do not carry as much statistical weight as the conclusions about the other approaches, which were always based on five valid tests. To confirm the effect the matchstick approach has on G_{init} and G_{prop}, future research would need to replicate the fracture toughness tests, ensuring there are five valid tests for each of the three considered overlap values (5 mm, 10 mm and 20 mm).

Finally, the fiber bridging analysis could be improved. In the current project, it is based on roughness analysis of the fracture surfaces. This causes inaccuracies when fiber bridging does not occur over the whole surface, and does not account for the load the fibres can sustain, as pointed out in Chapter 5. Since fiber bridging is an important toughening mechanism in Vectra A950, a more profound understanding of this phenomenon would be critical for the further use of the material. One way to achieve that would be to perform a complete bridging zone analysis using traction-separation laws, such as the one performed by Nairn et al [26] to analyse wood.

7.2. Future research directions

This project's main objective is to improve the interlaminar Mode I fracture toughness of FDM-printed Vectra A950. Mode I was chosen for study since it is a very common fracture mode and since the shear fracture modes (II and III) require more energy, and are thus less critical. However, for LCP to find widespread use in the aerospace industry, its performance along the other failure modes would also need to be quantified. The same holds for its performance in the Mixed Modes I/II, II/III and I/III.

Of the toughening approaches studied, the matchstick approach and the sawtooth layers show promise in improving the Mode I toughness of LCP. However, only three values of the control parameter were tested in each case. It would be beneficial to test samples with higher matchstick overlap lengths and larger wave sharpness angles to see if they perform even better than the ones tested in this research.

Z-pinning, in contrast, was proven to be ineffective. Nevertheless, it is unclear if that is due to the concept itself not combining well with additive manufacturing, or due to its current implementation. More experimentation is needed to reach a definitive conclusion. One direction future research can take is printing pins that span the whole thickness

of the sample, instead of shorter pins that only span a few layers like in the current research. This may avoid the issue of the drop-shaped z-pins.

Finally, there are further toughening approaches existing in nature that can be adapted for use with FDM-printed LCP, which were not adopted by this project either due to being less practical than the approaches chosen, or due to reinforcing a fracture mode different than interlaminar Mode I. Among these are the Bouligand structures in the dactyl clubs of mantis shrimps, which Mencattelli and Pinho have already adapted for composites [3]. These structures are effective at shielding structures from forces acting perpendicular to the layers, and can be useful to make LCP resistant to impact loads from hailstones, for example. The Bouligand structures and other bio-inspired toughening approaches can be applied alongside or separately from those studied in the current project, to tackle any loading case in which LCP does not perform well on its own. With these toughening approaches, liquid crystalline polymers become versatile enough to warrant consideration for use in primary components in the aerospace industry.

Bibliography

[1] S. Gantenbein, K. Masania, W. Woigk, J. Sesseg, T. Tervoort, and A. Studart, "Three-dimensional printing of hierarchical liquid-crystal-polymer structures," *Nature*, vol. 561, pp. 226–230, 7722 2018.

[2] S. N. Patek, W. L. Korff, R. L. Caldwell, S. N. Patek, W. L. Korff, and R. L. Caldwell, "Biomechanics: Deadly strike mechanism of a mantis shrimp," *Nature*, vol. 428, pp. 819–820, 6985 Apr. 2004, ISSN: 0028-0836. DOI: 10.1038/428819A. [Online]. Available: https://ui.adsabs.harvard.edu/abs/2004Natur.428..819P/abstract.

[3] L. Mencattelli and S. T. Pinho, "Herringbone-bouligand cfrp structures: A new tailorable damage-tolerant solution for damage containment and reduced delaminations," *Composites Science and Technology*, vol. 190, Apr. 2020, ISSN: 02663538.

[4] S. Gantenbein, C. Mascolo, C. Houriet, *et al.*, "Spin-printing of liquid crystal polymer into recyclable and strong all-fiber materials," *Advanced Functional Materials*, 2021. DOI: 10.1002/adfm.202104574.

[5] M. Heidari-Rarani, M. Rafiee-Afarani, and A. M. Zahedi, "Mechanical characterization of fdm 3d printing of continuous carbon fiber reinforced pla composites," *Composites Part B: Engineering*, vol. 175, p. 107 147, Oct. 2019, ISSN: 1359-8368.

[6] E. Yasa and K. Ersoy, "A review of the additive manufacturing of fiber reinforced polymer matrix composites," in *2018 International Solid Freeform Fabrication Symposium*, University of Texas at Austin, 2018.

[7] R. J. Young and P. A. Lovell, *Introduction to Polymers*, 3rd. CRC Press, 2011.

[8] C. Tai-Shung, *Thermotropic liquid crystal polymers : thin-film polymerization, characterization, blends, and applications*. Technomic Pub. Co, 2001, p. 364, ISBN: 1566769434.

[9] A. J. Brunner, "Fracture mechanics characterization of polymer composites for aerospace applications," *Polymer Composites in the Aerospace Industry*, pp. 191–230, 2015. DOI: 10.1016/B978-0-85709-523-7.00008-6.

[10] M. J. Laffan, *Testing the toughness of polymer matrix composites*. Elsevier Ltd, Jan. 2012, pp. 110–128, ISBN: 9781845697501.

[11] A. J. Brunner, B. R. Blackman, and P. Davies, "A status report on delamination resistance testing of polymer-matrix composites," *Engineering Fracture Mechanics*, vol. 75, pp. 2779–2794, 9 Jun. 2008, ISSN: 00137944. DOI: 10.1016/J.ENGFRACMECH.2007.03.012.

[12] Z. Jia and L. Wang, "3d printing of biomimetic composites with improved fracture toughness," *Acta Materialia*, vol. 173, pp. 61–73, Jul. 2019, ISSN: 13596454. DOI: 10.1016/j.actamat.2019.04.052.

[13] G. Cherepanov, "The propagation of cracks in a continuous medium," *Journal of Applied Mathematics and Mechanics*, vol. 31, no. 3, pp. 503–512, 1967.

[14] J. R. Rice, "A Path Independent Integral and the Approximate Analysis of Strain Concentration by Notches and Cracks," *Journal of Applied Mechanics*, vol. 35, no. 2, pp. 379–386, Jun. 1968, ISSN: 0021-8936.

[15] A. Koko, P. Earp, T. Wigger, J. Tong, and T. Marrow, "J-integral analysis: An edxd and dic comparative study for a fatigue crack," *International Journal of Fatigue*, vol. 134, May 2020. DOI: 10.1016/j.ijfatigue.2020.105474.

[16] P. Nevasmaa, P. Karjalainen-Roikonen, A. Laukkanen, *et al.*, "Fracture characteristics of new ultra-high-strength steel with yield strengths 900-960 mpa," in *2nd International Conference Super-High Strength Steels (SHSS)*, Peschiera del Garda, 2010.

[17] M. S. B. M. Rehan, J. Rousseau, S. Fontaine, and X. J. Gong, "Experimental study of the influence of ply orientation on dcb mode-i delamination behavior by using multidirectional fully isotropic carbon/epoxy laminates," *Composite Structures*, vol. 161, pp. 1–7, Feb. 2017, ISSN: 02638223. DOI: 10.1016/J.COMPSTRUCT.2016.11.036.

[18] M. R. Aliha, H. Ghazi, and F. Ataei, "Experimental fracture resistance study for cracked bovine femur bone samples," *Frattura ed Integrità Strutturale*, vol. 13, pp. 602–612, 50 Sep. 2019, ISSN: 1971-8993. DOI: 10.3221/IGF-ESIS.50.51.

[19] D. T. Schmieden, "Imitating nature to produce nacre-inspired composite materials with bacteria," *Dissertation at Delft University of Technology*, 2019.

[20] N. Zhang, S. Yang, L. Xiong, Y. Hong, and Y. Chen, "Nanoscale toughening mechanism of nacre tablet," *Journal of the Mechanical Behavior of Biomedical Materials*, vol. 53, pp. 200–209, Jan. 2016, ISSN: 18780180. DOI: 10.1016/J.JMBBM.2015.08.020.

[21] E. K. Gamstedt, T. K. Bader, and K. D. Borst, "Mixed numerical-experimental methods in wood micromechanics," *Wood Science and Technology*, vol. 47, pp. 183–202, 1 Jan. 2013, ISSN: 00437719.

[22] M.-C. Maaß, S. Saleh, H. Militz, *et al.*, "The structural origins of wood cell wall toughness," *Advanced Materials*, vol. 32, p. 1 907 693, 16 Apr. 2020, ISSN: 1521-4095.

[23] S. Pech, M. Lukacevic, and J. Füssl, "Validation of a hybrid multi-phase field model for fracture of wood," *Engineering Fracture Mechanics*, vol. 275, p. 108 819, Nov. 2022, ISSN: 0013-7944.

[24] S. Vasic and I. Smith, "Bridging crack model for fracture of spruce," *Engineering Fracture Mechanics*, vol. 69, pp. 745–760, 6 Apr. 2002, ISSN: 0013-7944.

[25] B. Mirzaei, A. Sinha, and J. A. Nairn, "Measuring and modeling fiber bridging: Application to wood and wood composites exposed to moisture cycling," *Composites Science and Technology*, vol. 128, pp. 65–74, May 2016, ISSN: 0266-3538. [Online]. Available: https://linkinghub.elsevier.com/retrieve/pii/S0266353816301051.

[26] J. Nairn and N. Matsumoto, "Fracture modeling of crack propagation in wood and wood composites including crack tip processes and fiber bridging mechanics," in *Proceedings of the 12th International Conference on Fracture, Ottawa, July*, 2009, pp. 12–17.

[27] A. P. Mouritz, "Review of z-pinned composite laminates," *Composites Part A: Applied Science and Manufacturing*, vol. 38, pp. 2383–2397, 12 Dec. 2007, ISSN: 1359835X. DOI: 10.1016/j.compositesa.2007.08.016.

[28] C. Duty, J. Failla, S. Kim, T. Smith, J. Lindahl, and V. Kunc, "Z-pinning approach for 3d printing mechanically isotropic materials," *Additive Manufacturing*, vol. 27, pp. 175–184, May 2019, ISSN: 2214-8604. DOI: 10.1016/J.ADDMA.2019.03.007.

[29] G. Gu, F. Libonati, S. D. Wettermark, and M. J. Buehler, "Printing nature: Unraveling the role of nacre's mineral bridges," *Journal of the Mechanical Behavior of Biomedical Materials*, vol. 76, pp. 135–144, 2017. [Online]. Available: https://www.sciencedirect.com/science/article/pii/S1751616117301959.

[30] L. Djumas, A. Molotnikov, G. P. Simon, and Y. Estrin, "Enhanced mechanical performance of bio-inspired hybrid structures utilising topological interlocking geometry," *Scientific Reports*, vol. 6, May 2016, ISSN: 20452322. DOI: 10.1038/SREP26706.

[31] V. Nguyen-Van, S. Wickramasinghe, A. Ghazlan, H. Nguyen-Xuan, and P. Tran, "Uniaxial and biaxial bioinspired interlocking composite panels subjected to dynamic loadings," *Thin-Walled Structures*, vol. 157, p. 107 023, Dec. 2020, ISSN: 0263-8231. DOI: 10.1016/J.TWS.2020.107023.

[32] Z. Ding, B. Wang, H. Xiao, and Y. Duan, "Hybrid bio-inspired structure based on nacre and woodpecker beak for enhanced mechanical performance," *Polymers*, vol. 13, p. 3681, 21 Oct. 2021, ISSN: 2073-4360. DOI: 10.3390/POLYM13213681. [Online]. Available: https://www.mdpi.com/2073-4360/13/21/3681.

[33] F. A. Cordisco, P. D. Zavattieri, L. G. Hector, and B. E. Carlson, "Mode i fracture along adhesively bonded sinusoidal interfaces," *International Journal of Solids and Structures*, vol. 83, pp. 45–64, Apr. 2016, ISSN: 0020-7683.

[34] P. D. Zavattieri, L. G. Hector, and A. F. Bower, "Determination of the effective mode-i toughness of a sinusoidal interface between two elastic solids," *International Journal of Fracture*, vol. 145, pp. 167–180, 3 Sep. 2007, ISSN: 15732673.

[35] A. Argüelles, J. Viña, A. F. Canteli, and J. Bonhomme, "Fatigue delamination, initiation, and growth, under mode i and ii of fracture in a carbon-fiber epoxy composite," *Polymer Composites*, vol. 31, pp. 700–706, 4 Apr. 2010, ISSN: 1548-0569. DOI: 10.1002/PC.20855.

[36] C. Houriet, "Multi-axis printing of hierarchically structured liquid crystal polymers: A PhD research proposal (unpublished),"

[37] Z. Zhang, D. Yavas, Q. Liu, and D. Wu, "Effect of build orientation and raster pattern on the fracture behavior of carbon fiber reinforced polymer composites fabricated by additive manufacturing," *Additive Manufacturing*, vol. 47, Nov. 2021, ISSN: 2214-8604.

[38] J. M. Pappas, A. R. Thakur, M. C. Leu, and X. Dong, "A comparative study of pellet-based extrusion deposition of short, long, and continuous carbon fiber-reinforced polymer composites for large-scale additive manufacturing," *Journal of Manufacturing Science and Engineering, Transactions of the ASME*, vol. 143, 7 Jul. 2021, ISSN: 15288935.

[39] B. Ezair, S. Fuhrmann, and G. Elber, "Volumetric covering print-paths for additive manufacturing of 3d models," *Computer-Aided Design*, vol. 100, pp. 1–13, Jul. 2018, ISSN: 0010-4485.